The histone acetyltransferase HBO1 (KAT7) promotes efficient tip cell sprouting during angiogenesis

Zoe L Grant[1,2,7], Peter F Hickey[1,2], Waruni Abeysekera[1,2], Lachlan Whitehead[1,2], Sabrina M Lewis[1,2], Robert CA Symons[3,4,5], Tracey M Baldwin[1], Daniela Amann-Zalcenstein[1,2], Alexandra L Garnham[1,2], Gordon K Smyth[1,6], Tim Thomas[1,2], Anne K Voss[1,2*], Leigh Coultas[1,2*].

[1]The Walter and Eliza Hall Institute of Medical Research, 1G Royal Parade, Parkville, Victoria 3052, Australia

[2]Department of Medical Biology, University of Melbourne, VIC 3052 Australia

[3]Department of Optometry and Vision Sciences, University of Melbourne, Parkville, 3010 Australia

[4]Department of Surgery, University of Melbourne, Parkville, 3010 Australia

[5]Department of Ophthalmology, Royal Melbourne Hospital, Parkville, 3050 Australia

[6]School of Mathematics and Statistics, University of Melbourne, VIC 3010 Australia

[7]Current address: Gladstone Institutes, San Francisco, CA 94158 USA

*these authors contributed equally. Correspondence should be addressed to Leigh Coultas, email: lcoultas@wehi.edu.au and Anne K. Voss, email: avoss@wehi.edu.au

Key words: angiogenesis, histone acetylation, endothelial cell, single-cell RNA-sequencing, sprouting

Abstract

Blood vessel growth and remodelling are essential during embryonic development and disease pathogenesis. The diversity of endothelial cells (ECs) is transcriptionally evident and ECs undergo dynamic changes in gene expression during vessel growth and remodelling. Here, we investigated the role of the histone acetyltransferase HBO1 (KAT7), which is important for activating genes during development and histone H3 lysine 14 acetylation (H3K14ac). Loss of HBO1 and H3K14ac impaired developmental sprouting angiogenesis and reduced pathological EC overgrowth in the retinal endothelium. Single-cell RNA-sequencing of retinal ECs revealed an increased abundance of tip cells in *Hbo1* deleted retinas, which lead to EC overcrowding in the retinal sprouting front and prevented efficient tip cell migration. We found that H3K14ac was highly abundant in the endothelial genome in

both intra- and intergenic regions suggesting that the role of HBO1 is as a genome organiser that promotes efficient tip cell behaviour necessary for sprouting angiogenesis.

Introduction

The expansion of blood vessel networks by angiogenesis is critical for matching blood supply to the metabolic demands of growing tissues. In adult tissues, blood vessels and the endothelial cells (ECs) that line them generally remain in a quiescent state. However, the reactivation of angiogenesis is a hallmark of a number of diseases including cancer and vision-threatening eye diseases (Ferrara and Adamis, 2016, Miller et al., 2013). Sprouting angiogenesis and subsequent vessel remodelling generates diverse EC identities (Potente and Makinen, 2017) and is a major driver of vessel growth in both developmental and pathological contexts. Pro-angiogenic signals such as vascular endothelial growth factor (VEGFA) stimulate the formation of vessel sprouts. Vessel sprouts are made up of two types of EC: migratory tip cells that guide growing sprouts and trailing stalk cells that proliferate to contribute new cells to growing sprouts (Gerhardt et al., 2003). Tip and stalk cells exist transiently, switching identities during angiogenesis (Jakobsson et al., 2010, Arima et al., 2011), with tip cells ultimately directed to the growing arteries (Pitulescu et al., 2017, Xu et al., 2014). The new vessels formed during sprouting angiogenesis are immature and must be remodelled into hierarchical, mature vessel networks. This includes establishment of arteries, veins and capillaries and defined identity of ECs within each of these (Potente et al., 2011).

The diversity of these distinct EC types is evident at a transcriptional level, with each type exhibiting gene expression profiles that distinguish them from another. Large scale characterisation of transcriptional heterogeneity of EC populations has been made possible by advances in single-cell RNA-sequencing (scRNA-seq) (Jakab and Augustin, 2020). This has enabled profiling of EC heterogeneity in a range of tissues, including within quiescent adult tissues (Vanlandewijck et al., 2018, Kalucka et al., 2020, Tikhonova et al., 2019, Lukowski et al., 2019), in the activated endothelium of tumours (Goveia et al., 2020, Zhao et al., 2018) and in some developing vascular beds, including in the brain (Sabbagh et al., 2018) and coronary arteries (Su et al., 2018). These studies have also highlighted key transcription factors that are expressed within each subtype. The actions of DNA-binding transcription factors are essential for cell-type specific gene expression; however, the compacted nature of

chromatin is refractory to these interactions. This requires the additional actions of chromatin-associating enzymes that modify chromatin. Snapshots of EC heterogeneity obtained from scRNA-seq do not provide information about the dynamic interactions of these enzymes with chromatin that enable gene expression patterns to be established. Furthermore, the plasticity and fate switching that occurs in the immature vessel networks to enable efficient vessel network expansion and remodelling requires that ECs change their gene expression patterns. This is particularly relevant in the context of tip and stalk cell shuffling, as entering or exiting the transcriptionally distinct tip cell fate would involve dynamic changes in gene expression (del Toro et al., 2010, Strasser et al., 2010).

Histone acetyltransferases (HATs) are chromatin-modifying enzymes that dynamically regulate gene expression by catalysing the transfer of an acetyl group to histone tail lysine residues. The resulting histone acetylation mark is typically correlated with active gene expression (Karmodiya et al., 2012, Wang et al., 2009). Various histone lysine residues can be acetylated with differences in genome abundance, function and downstream consequences. Here, we focussed on HBO1 (also known as KAT7 or MYST2) that is exclusively required for histone H3 lysine 14 acetylation (H3K14ac) (Kueh et al., 2020, Kueh et al., 2011), the second most abundant mark in the human genome with >15% of sites acetylated (Feller et al., 2015, Hansen et al., 2019). Of interest, HBO1 has an essential role in regulating patterning gene expression necessary for determining embryonic structures and cell types during development (Kueh et al., 2011). Deletion of *Hbo1* leads to a global loss of H3K14ac and a failure of *de novo* expression of lineage specific genes required for post-gastrulation differentiation. This includes failure to express the genes *Tie1*, *Tie2* and *Vegfr2* that are necessary for patterning the vasculature (Kueh et al., 2011). In addition, *Hbo1*$^{-/-}$ embryos display a range of defects, including but not limited to abnormal yolk sac vasculature and dilated dorsal aortae and pharyngeal arch arteries (Kueh et al., 2011). In zebrafish, the *Hbo1* orthologue *kat7b* was shown to be required for normal expression of *Vegfr2* and necessary to promote EC migration and vessel sprouting (Yan et al., 2018). Together, the observation that HBO1 is necessary for lineage specific gene expression accompanying differentiation and the vascular phenotype observed in *kat7b* morphants and *Hbo1*$^{-/-}$ embryos posit a role for HBO1 in regulating gene expression patterns required for EC differentiation during angiogenesis.

Using tissue-specific conditional deletion of *Hbo1* in mice, scRNA-seq, chromatin immunoprecipitation and sequencing, whole-mount immunofluorescence and an oxygen-induced retinopathy model, we have investigated the role of HBO1 in establishing the identity of ECs involved in angiogenesis in the mouse retina during post-natal development and in a disease model.

Results

HBO1 promotes sprouting angiogenesis

The neonatal mouse retina is a widely used model of angiogenesis, in which both vessel sprouting in response to pro-angiogenic factors and subsequent vessel network remodelling occur in parallel (Fig. 1A). EC subtypes involved in both aspects can be readily identified. To study the EC-autonomous role for HBO1 during sprouting angiogenesis, mice carrying *Hbo1* conditional alleles (Kueh et al., 2011) were crossed to those expressing the tamoxifen inducible, endothelial specific *Cdh5(PAC)-creER*^{T2} transgene (Wang et al., 2010). Pups were administered tamoxifen at postnatal day (P)1 and P2 to induce nuclear translocation of cre-recombinase and EC-specific deletion of exon 1 of *Hbo1* (Fig. 1B), hereafter referred to as *Hbo1*$^{iEC/iEC}$ mice. The genotypes of control mice included *Hbo1*$^{fl/+}$*;Cdh5(PAC)-creER*$^{T2+}$ (heterozygote following tamoxifen administration), *Hbo1*$^{fl/+}$ and *Hbo1*$^{fl/fl}$. Deletion of *Hbo1* resulted in a 2.7-fold reduction in endothelial *Hbo1* expression in lung ECs (Fig. 1C). H3K14 is the major acetylation target of HBO1 during mouse embryonic development and in human cell lines (Kueh et al., 2011, Kueh et al., 2020). Congruently, *Hbo1*$^{iEC/iEC}$ mice showed a significant reduction in endothelial H3K14ac compared to control mice (Fig. 1D,E). The P6 retina of *Hbo1*$^{iEC/iEC}$ mice displayed impaired angiogenic vessel growth as shown by reduced vessel area and radial vessel outgrowth as compared to control mice (Fig. 1F-H). Furthermore, the density of the vessel network formed was reduced in *Hbo1*$^{iEC/iEC}$ mice as shown by fewer vessel branchpoints and vessel segments (Fig. 1I,J). The patterning of arteries and veins was normal in *Hbo1*$^{iEC/iEC}$ retinas based on known morphological differences (Crist et al., 2017) and we did not observe any incidence of either vessel crossing over the other (Fig. 1F).

Reduced pathological angiogenesis in the absence of HBO1

Similar mechanisms can contribute to both developmental and pathological vessel growth (Dubrac et al., 2016, Raimondi et al., 2014, Rama et al., 2015). We used the oxygen-induced retinopathy (OIR) model to determine whether HBO1 was also important for pathological vessel growth. Mice were exposed to high oxygen for five days from P7, leading to vaso-obliteration of the central retina, which induces VEGFA-dependent pathological neovascular growth (Lee et al., 2013, Aiello et al., 1995). *Hbo1*$^{iEC/iEC}$ mutation was induced following exposure to high oxygen and retinas were then examined at the peak of pathological neovascular growth at P17 (Fig. 2A). We have previously established that neovascular lesions stain brightly for the basement membrane protein collagen IV (Grant et al., 2020). Staining for collagen IV revealed a significant reduction in pathological neovascular area in *Hbo1*$^{iEC/iEC}$ mice compared to controls (Fig. 2B,C), suggesting that HBO1 was also required for pathological vessel growth. Consistent with the developmental angiogenesis defect, *Hbo1*$^{iEC/iEC}$ retinas had a significantly increased vaso-obliterated area compared to controls (Fig. 2B,D), a region that is revascularised by sprouting angiogenesis from the unaffected peripheral vessels. The results from the OIR model support a necessary role for HBO1 in regulating both developmental and pathological vessel growth.

HBO1 is not essential for EC proliferation, EC apoptosis, vessel remodelling or maintaining vessel patterning

HBO1 has been shown to regulate proliferation in other cell types (Johmura et al., 2008, Wu and Liu, 2008). To assess proliferation, P6 mice were labelled for 2 h with the thymidine nucleoside analogue 5-ethynyl-2'-deoxyuridine (EdU), which is incorporated into newly synthesised DNA during S phase of the cell cycle. Proliferation rates in *Hbo1*$^{iEC/iEC}$ retinas were not significantly different from control mice (Fig. S1A,B). Further supporting this, the number of ECs relative to vessel area across the retina was unchanged between control and *Hbo1*$^{iEC/iEC}$ mice (Fig. S1C). During sprouting angiogenesis, the initially dense vessel plexus remodels into a hierarchical network involving both apoptosis dependent and independent vessel regression (Watson et al., 2017, Grant et al., 2020). We assessed apoptosis by staining for cleaved (active) caspase 3 and found that *Hbo1*$^{iEC/iEC}$ mice showed normal levels of endothelial apoptosis (Fig. S1D,E). We also found that vessel regression was unchanged in *Hbo1*$^{iEC/iEC}$ retinas (Fig. S1D,F). These results suggest that defects in proliferation or aberrant vessel pruning do not account for reduced vascularisation in *Hbo1*$^{iEC/iEC}$ retinas.

HBO1 was not required for vessel maintenance in adult tissues, as deletion of *Hbo1* at 6 weeks of age had no effect on the vasculature (Fig. S2A-D). Interestingly, H3K14ac expression was barely detectable in adult ECs from control retinas compared to surrounding cells and this was not reduced further in *Hbo1*$^{iEC/iEC}$ retinas (Fig. S2E). We confirmed that cre-recombinase was active in these mice by intercrossing the cre-inducible, cell membrane-targeted EGFP reporter allele *mTmG* (Muzumdar et al., 2007) into these mice, which leads to EGFP expression in ECs and found extensive EGFP expression in ECs of both control and *Hbo1*$^{iEC/iEC}$ genotypes (Fig. S2F). Despite reduced H3K14ac in adults, we found that *Hbo1* mRNA levels were consistent across all ages from P6-50 in a publicly available developmental retinal EC RNA-seq dataset (Jeong et al., 2017) (Fig. S2G). Taken together, these findings suggest that HBO1 is not required during the neonatal remodelling process or maintaining vessel patterning in established vessel networks.

Profiling retinal EC transcriptomes by single cell RNA-sequencing

To investigate our hypothesis that HBO1 would be necessary for specifying EC identity and whether this could explain the phenotype caused by EC-specific loss of HBO1 in the retina, we first established the transcriptional heterogeneity of ECs within the postnatal retina at a single cell level. We sorted ECs from dissociated P6 retinas into 384-well plates and performed single-cell RNA-sequencing (scRNA-seq) using CEL-Seq2 (Hashimshony et al., 2016). For this we used heterozygous control and *Hbo1*$^{iEC/iEC}$ mice crossed with the *mTmG* reporter and treated with tamoxifen at P1 and P2 (hereafter *Control*$^{iEC/+}$*;mTmG* and *Hbo1*$^{iEC/iEC}$*;mTmG,* respectively).We defined ECs as PECAM1^{+}EGFP^{+}, thereby isolating only those ECs in which cre recombination had taken place. We sequenced 1733 cells with an average sequencing depth of 13222 reads per cell and 3466 genes per cell. After quality controlling for the number of detected genes and mitochondrial and spike-in RNA reads (Fig. S3A), 1393 cells were pooled, batch-corrected, clustered and visualised using uniform manifold approximation and projection (UMAP) plots (Fig. 3A and Fig. S3B,C). All cells expressed high levels of endothelial markers *Pecam1*, *Cdh5* and *Vegfr2* (Fig. S3D). Consistent with the neural nature of the retina, retinal ECs were transcriptionally reminiscent of adult brain ECs, including robust expression of the brain EC-specific marker *Pglyrp1* (Kalucka et al., 2020) (Fig. S3E,F). Clustering analysis identified seven clusters (Fig. 3A, Fig. S4A,B) that were annotated based on known EC-subtype markers such as *Gja4* for arterial ECs (Fang et al., 2017), *Aplnr* for venous ECs (Saint-Geniez et al., 2003) and *Esm1* for tip cells (Rocha et al., 2014), in addition to recent other endothelial subtype marker gene

lists (Kalucka et al., 2020, Goveia et al., 2020) (Fig. 3B and Fig. S4A,B). Capillary ECs exhibit tissue specific gene expression (Kalucka et al., 2020). Therefore, we annotated capillary ECs using brain capillary markers, such as *Spock2* for all capillary ECs (Kalucka et al., 2020), arterial capillary marker *Tgfb2* and venous capillary marker *Tfrc* (Vanlandewijck et al., 2018) (Fig. 3B). Three clusters expressed venous/capillary markers and no proliferation markers (Fig. 3A, Fig. S4A). For clarity of presentation and downstream analysis, we combined these three clusters. We were unable to discern a discrete stalk cell population even while using known stalk cell expressed genes, including those activated by Notch and TGFb/BMP signalling (Moya et al., 2012, Larrivee et al., 2012, Strasser et al., 2010), and other genes expressed by stalk-like cells identified by scRNA-seq of tumour ECs (Zhao et al., 2018) (Fig. S4A). In contrast to adult tissue vasculature in which very few ECs were proliferating (Kalucka et al., 2020), we identified two proliferative clusters based on cyclin gene expression that accounted for about 30% of all cells analysed (Fig. S4A-C). Most of the ECs within the proliferative clusters were of venous/capillary identity (Fig. 3B). This is consistent with these ECs being highly proliferative in the postnatal retina (Ehling et al., 2013). Supporting the annotation of distinct EC types, heatmap analysis of top-ranking marker genes revealed distinct transcriptional signatures of ECs within each cluster (Fig. 3C and Table S1). Thus, we were able to interrogate intra-tissue endothelial heterogeneity in the postnatal retina, identifying tip cells, which predominate in the sprouting region and arterial and venous ECs, which predominate in the remodelling region of the neonatal retina.

Hbo1 deficient retinas have increased expression of tip cell genes and an expanded tip cell compartment

H3K14ac is a mark correlated with active gene transcription (Karmodiya et al., 2012). As HBO1 is essential for H3K14ac in mouse cells (Kueh et al., 2011, Mishima et al., 2011), human cells lines (Kueh et al., 2020) and mouse retinal ECs (Fig. 1D,E), we predicted that loss of HBO1 could affect gene expression. Given the relatively small number of cells available for scRNA-seq per animal in the neonatal retina, which was further reduced when the cells were divided up into clusters, we first examined the effects of loss of HBO1 on gene expression ignoring the cluster identity. Neonatal retinal ECs from *Hbo1*$^{iEC/iEC}$ mice had 92 downregulated and 61 upregulated genes with false discovery rate (FDR) <0.05 compared to *Control*$^{iEC/+}$*;mTmG* ECs (Fig. 4A,B and Table S2). Differentially expressed genes in the venous/capillary cluster (which contained the most cells), accounted for about 40% of the differentially expressed genes identified ignoring cluster identity (Fig. S5A). Appropriate

deletion of the *Hbo1* gene was confirmed by a reduction in *Hbo1* mRNA, but there was no change in the expression of other HAT genes in the absence of HBO1 (Fig. S5B). Mirroring the normal artery and vein patterning in the *Hbo1*$^{iEC/iEC}$ retina, we found the mRNA levels of artery and vein markers were not consistently up or downregulated in *Hbo1*$^{iEC/iEC}$*;mTmG* retinal ECs (Fig. S5C,D). In contrast, we found that many tip cell expressed genes, including *Esm1*, *Igfbp3* and *Cxcr4* (del Toro et al., 2010, Strasser et al., 2010), were more highly expressed in *Hbo1*$^{iEC/iEC}$*;mTmG* ECs compared to *Control*$^{iEC/+}$*;mTmG* ECs (Fig. 4C). In addition, *Hbo1*$^{iEC/iEC}$*;mTmG* retinas tended to have a higher proportion of tip cells expressing tip cell markers highly (Fig. 4D, Fig. S5E). We found that upregulated genes were associated with gene ontology (GO) terms for *angiogenesis, blood vessel/vasculature development,* and *cell adhesion* and were amongst the most significantly enriched in *Hbo1*$^{iEC/iEC}$*;mTmG* mice (Fig. 4E,F, Table S3). In contrast, many of the downregulated genes encoded transport proteins from solute carrier SLC families (Table S2) and we saw a corresponding predominance of downregulated GO terms relating to transport of small molecules and metabolites (Fig. 4E, Fig. S5F and Table S3). Overall, these data provide insight into the processes that are dependent on HBO1 during angiogenesis. Deletion of *Hbo1* did not affect genes in the Notch, VEGF, FOXO, TGF-beta and HIF1 signalling pathways in a directional manner (Fig. S5G and not shown). To understand if there was an accumulation or depletion of a particular subtype of EC, we also analysed the differential abundance per genotype within each cluster identified by scRNA-seq. We found that *Hbo1*$^{iEC/iEC}$*;mTmG* retinas had an enrichment of cells in the tip cell cluster (Fig. 4G). Consistent with our EdU analysis showing no proliferation defect in *Hbo1*$^{iEC/iEC}$ retinas, we found ECs in each proliferative cluster were similarly abundant in both genotypes (Fig. 4G). Overall, differential analysis of our scRNA-seq data suggested that tip cell genes were upregulated per cell and that there was an accumulation of tip cells in retinas with *Hbo1* deleted.

H3K14ac is widely distributed across the endothelial genome but enriched at genes required for vascular development

Previous studies have shown that H3K14ac is a highly abundant mark in the genome (Feller et al., 2015, Hansen et al., 2019). To understand whether its occupancy correlates with particular regions of the activated endothelial genome, we performed chromatin-immunoprecipitation and sequencing (ChIP-seq) in human umbilical vein ECs (HUVECs). To reproduce angiogenic conditions, HUVECs were grown in low oxygen (3% oxygen) and stimulated with VEGFA prior to harvesting for ChIP (Fig. S6A). There were a large number

of genes where H3K14ac was enriched compared to histone H3 (Table S4), including in endothelial genes such as *PECAM1* and *DLL4* (Fig. 5A and Fig. S6B). Supporting this, amongst the most significant GO biological processes terms for gene bodies enriched with H3K14ac above histone H3 included *angiogenesis* and *blood vessel development* and *blood vessel morphogenesis* (Fig. 5B, Table S5), highlighting a critical role for H3K14ac in behaviours essential for vascular development. H3K14ac depleted regions were associated with GO terms relating to neural processes such as *regulation of postsynaptic membrane potential* and *GABAergic synaptic transmission*, likely reflecting the repressed state of genes specific to other tissues (Fig. S6C, Table S5). We compared genes with enriched H3K14ac to genes previously found to be highly expressed in activated HUVECs (Zhang et al., 2013). We found that genes highly expressed in HUVECs were significantly enriched for H3K14ac, whereas lowly expressed genes were depleted for H3K14ac (Fig. 5C). Consistent with the expression pattern of HBO1 occupancy (Saksouk et al., 2009, Avvakumov et al., 2012, Lalonde et al., 2013), we found that the level of H3K14ac immediately downstream of the transcription start site (TSS) correlated positively with gene expression (Fig. 5D). Interestingly, H3K14ac was widely distributed across the genome with only ~35% reads mapping to gene bodies (Fig. 5E, Fig. S6D).

HBO1 is required for normal tip cell sprouting

As the scRNA-seq suggested an increase in the proportion of tip cells in the *Hbo1*$^{iEC/iEC}$ retinas (Fig. 4G), we examined tip cell numbers and function in the *Hbo1*$^{iEC/iEC}$ retinas. While control mice had many vessel sprouts indicative of tip cell activity extending out from the vessel front, *Hbo1*$^{iEC/iEC}$ retinas had a blunted appearance (Fig. 6A) and a significant decrease in the number of vessel sprouts (Fig. 6B). However, the sprouts that did form were on average the same length between control and *Hbo1*$^{iEC/iEC}$ mice (Fig. 6C). Following the vascularisation of the superficial layer of the retina, vessels sprout downwards to form additional vessel layers deeper within the retina, beginning around P7. While the superficial layer of *Hbo1*$^{iEC/iEC}$ retinas was vascularised to the same extent as control retinas by P10 (Fig. S7A,B), sprouting into the deeper layers of the retina was impaired as evidenced by a reduction in the formation of the deep vessel layer in P10 *Hbo1*$^{iEC/iEC}$ mice (Fig. S7C). These findings confirm a general vessel sprouting defect.

To determine if tip cell identity was correctly specified in the absence of HBO1, retinas were stained for the VEGFA-responsive marker ESM1, which is selectively expressed by tip cells in the sprouting retinal vasculature (Rocha et al., 2014). We found that ECs at the sprout front expressed ESM1, indicating that they were able to respond to VEGFA signalling and adopt tip cell identity (Fig. 6A). Consistent with this, staining for another tip cell marker, DLL4, showed ECs at the sprouting front of *Hbo1*$^{iEC/iEC}$ retinas expressing DLL4, consistent with successful tip cell specification (Fig. S7D). ESM1+ ECs were normally distributed to the sprouting front of *Hbo1*$^{iEC/iEC}$ retinas, but there were significantly more of them than in control mice (Fig. 6A,D). Consistent with the increased *Esm1* mRNA levels detected by scRNA-seq, we found that expression of ESM1 protein in *Hbo1*$^{iEC/iEC}$ ESM1+ cells was increased compared to control ESM1+ cells (Fig. 6E). In contrast, the number of ECs expressing another tip cell marker, hypoxia responsive ANG2, was not significantly changed across the *Hbo1*$^{iEC/iEC}$ retina compared to controls (Fig. S7E,F). These results together with the scRNA-seq data suggest that the altered sprouting in *Hbo1*$^{iEC/iEC}$ mice was not due to a failure to specify tip cell identity, but may be due to an inability to form functional sprouts.

Hbo1 deleted tip cells fail to establish biased migration and accumulate in the sprouting front

HBO1 has been previously shown to promote EC migration using *in vitro* scratch-wound assays (Yan et al., 2018). Tip cells are highly migratory and a defect in this migratory behaviour could explain the reduced vessel sprouting observed in *Hbo1*$^{iEC/iEC}$ mutants. Tip cells achieve directed migration by establishing front-rear polarity, which occurs as the tip cell orients its Golgi apparatus towards the sprouting front relative to the nucleus (Moya et al., 2012, Franco et al., 2015, Dubrac et al., 2016) (Fig. 6F). To assess Golgi apparatus orientation in tip cells, we stained retinas with the Golgi apparatus marker GM130, the nuclear marker FLI1 and the tip cell marker ESM1. Consistent with previous findings (Dubrac et al., 2016), in control mice, most tip cells were preferentially polarised in the direction of sprout elongation (Fig. 6G,H). In contrast, *Hbo1*$^{iEC/iEC}$ tip cells did not display a polarity bias and Golgi apparatus were randomly aligned relative to the direction of sprout elongation (Fig. 6G,H), suggesting an impairment in sprout migration. Consistent with failed sprout migration, the sprouting front of *Hbo1*$^{iEC/iEC}$ retinas displayed increased EC density (Fig. 6G,I), corresponding to an increase in vessel width compared to control vessels (Fig. 6J). This is in contrast to vessels in the remodelling zone, which display normal EC density and vessel width (Fig. 6K,L), further supporting normal vessel remodelling in the absence of

HBO1. Together, these data suggest that in the absence of HBO1, tip cells fail to sprout and migrate normally, which leads to an accumulation of ECs within the sprouting front and a relative greater abundance of tip cells, as observed in the scRNA-seq data.

Discussion

Establishing distinct EC identity and function is crucial for the normal growth and patterning of the vasculature and involves changes in gene expression patterns. While ECs exhibit distinct identity at a transcriptional level, how these differences arise through the actions of chromatin-associating enzymes is not well understood. In this study, we investigated the involvement of the histone acetyltransferase HBO1 in EC identity specification. HBO1 is responsible for deposition of the second most abundant histone acetylation mark in the human genome, H3K14ac (Kueh et al., 2011, Kueh et al., 2020, Feller et al., 2015, Hansen et al., 2019). We found that H3K14ac was widely distributed across the human endothelial genome, and that deletion of *Hbo1* in mice reduced global H3K14ac. In the absence of H3K14ac and HBO1, retinal angiogenesis was impaired in both normal and pathological contexts. This was not due to a failure of tip cell specification but rather to an accumulation of tip cells, which were unable to collectively and efficiently organise to undergo directed migration.

HBO1 was previously implicated in the regulation of angiogenic EC migration in HUVECs and zebrafish (Yan et al., 2018). Our study represents the first to directly examine the role of a HAT during *in vivo* mammalian vascular development. Other studies have shown that the HAT activity of EP300 is necessary for transcription factor binding and activation of critical endothelial genes (Sacilotto et al., 2016, Shu et al., 2015), however, little is known about the cell-autonomous roles of other HATs during sprouting angiogenesis or vascular development more generally. Loss of the histone deacetylase activity of HDAC10 changes the ability of ECs to sprout *in vitro* (Duan et al., 2017), supporting the role of dynamically regulating histone acetylation marks to control gene expression patterns associated with changes to EC behaviour.

We generated single cell transcriptomic data using neonatal ECs to characterise the intra-tissue heterogeneity of the angiogenic retinal endothelium and studied the transcriptional changes due to deletion of *Hbo1*. Although we hypothesised that EC identity specification would be perturbed in the absence of HBO1, to our surprise, we instead found that EC fate was mostly established normally. In our scRNA-seq dataset, we observed proliferating, arterial and venous/capillary ECs clusters that were comprised of both genotypes in equal proportions, suggesting no consistent change in their identity specification. This was in accordance with the normal morphological patterning of arteries and veins observed in *Hbo1* deleted retinas. Interestingly, we found that tip cells were proportionally more abundant in *Hbo1* deleted retinas. We were unable to distinguish stalk cells, possibly due to overlapping gene expression patterns with arterial ECs, as both EC subtypes express Notch/TGFb/BMP activated genes, including *Hey1*, *Id1* and *Jag1* (Kalucka et al., 2020, Moya et al., 2012).

Our observation that tip cells were more abundant in the absence of HBO1 suggests that tip cells are the default EC type formed in the absence of HBO1-dependent chromatin organisation. This may be due to a role for HBO1 in both/either normally restraining tip cell fate or regulating exit from the tip cell fate during angiogenesis. A role for HBO1 in restraining tip cell fate is supported by the finding that tip cell expressed genes, including *Esm1*, *Cxcr4* and *Igfbp3*, were upregulated when *Hbo1* was deleted. We predict this occurs through the actions of an intermediate transcriptional repressor that depends on H3K14ac for association at these gene loci. Both *Esm1* and *Igfbp3* are expressed by tip cells (del Toro et al., 2010, Rocha et al., 2014) but deletion of these factors does not cause a failure to make tip cells (Dallinga et al., 2020, Rocha et al., 2014). In contrast, deletion of *Cxcr4* specifically from tip cells results in reduced likeliness of taking on the tip cell position (Pitulescu et al., 2017), suggesting that increased *Cxcr4* expression in *Hbo1* deleted retinas might contribute to the increase in tip cells. Alternatively, the defective migration observed in *Hbo1* tip cells may result in prolonged exposure to the elevated VEGFA levels normally present at the sprout front and subsequent increase in tip cell associated genes. The increase in tip cells may also suggest a failure of *Hbo1* deficient ECs to exit the tip cell phenotype. Classically, tip cell fate was thought to be laterally inhibited by activation of Notch signalling in stalk cells (Geudens and Gerhardt, 2011) or in a more inductive manner (Jakobsson et al., 2010, Bentley et al., 2014, Hasan et al., 2017, Pitulescu et al., 2017). Overactivation of Notch signalling leads to upregulation of tip cell markers *Esm1* and *Cxcr4* (Pitulescu et al., 2017), but reduced sprouting and vessel growth (Pitulescu et al., 2017, Phng et al., 2009, Izumi et al., 2012),

phenocopied by *Hbo1* deleted retinas. Gene set testing did not show a significant enrichment for upregulation of Notch signalling genes.

The reduction in vascular outgrowth and vessel sprouts in *Hbo1* deleted retinas may be caused by a defect in directed tip cell migration. Tip cells establish front-rear polarity during migration (Dubrac et al., 2016, Franco et al., 2015, Moya et al., 2012, Kim et al., 2019), thus we used front-rear polarity as a readout for an EC migration defect. In the absence of HBO1, tip cell front-rear polarity was disorganised relative to the direction of sprout elongation, suggesting a failure of biased migration that was consistent with the observed reduction in vessel growth. This was not due to defective FOXO1 signalling downstream of hypoxia, as shown by others (Kim et al., 2019). The *Odc1* gene encoding ornithine decarboxylase, a key enzyme involved in polyamine biosynthesis (Pegg, 2006), was one of two genes downregulated in tip cells. Ornithine decarboxylase activity has been reported to promote *in vitro* vessel sprouting and EC migration through regulation of actin cytoskeleton dynamics (Kucharzewska et al., 2010), raising the possibility that its dysregulation is one cause of the *Hbo1* migration phenotype. The observation that although the number of vessel sprouts was reduced, the average sprout length was not different between control and $Hbo1^{iEC/iEC}$ mice suggests that tip cells that become front-polarised are able to migrate normally. Therefore, our data suggest that directionless polarity decreases the efficiency by which the ECs can migrate and expand the vessel network. Neovessel formation in the OIR model is dependent on directed tip cell migration (Dubrac et al., 2016). Therefore, our findings that neovascular lesions were reduced in the absence of HBO1 are also likely to be explained by inefficient tip cell migration.

The role of HBO1 in promoting sprouting EC behaviour is in accordance with the findings of a previous study that assessed HBO1 knock down in HUVEC and zebrafish (Yan et al., 2018). However, our results do not support their conclusion that this was due to dysregulated VEGF signalling. We found that ECs in $Hbo1^{iEC/iEC}$ retinas expressed normal levels of *Vegfr2*. Additionally, $Hbo1^{iEC/iEC}$ mice were able to upregulate VEGFA responsive ESM1 and DLL4, suggesting that at least some VEGFR2 signalling outputs are normal. Owing to the small number of tip cells in our dataset, we could not examine gene expression in the tip cell cluster with statistical robustness and cannot rule out the possibility of altered VEGFA signalling pathway genes specifically in this cluster. Instead, based on the accumulation of ECs in the sprouting front and increased relative tip cell abundance when HBO1 is absent, we

suspect that the number of tip cells present, together with a migration defect, dictates sprouting efficiency.

Although several studies have suggested a role for HBO1 in regulating proliferation and DNA replication licensing (Iizuka and Stillman, 1999, Johmura et al., 2008, Wu and Liu, 2008), this role is disputed. We have previously shown that proliferation in mouse embryonic fibroblasts is not affected by loss of HBO1 (Kueh et al., 2011) and human MCF7, HEK293T and HeLa cells can proliferate without HBO1 (Kueh et al., 2020). Consistent with other *in vivo* studies of HBO1 (Kueh et al., 2011), we did not find HBO1 to be essential for endothelial proliferation by EdU labelling. Supporting this, our scRNA-seq data did not reveal any differences in proliferating cells or regulation of genes relating to proliferation.

The relative abundance of upregulated genes when *Hbo1* is deleted, as shown here in ECs and previously in HeLa cells (Kueh et al., 2020), suggests that the presence of H3K14ac at target genes is not simply for gene expression activation. Given the extensive occupancy of H3K14ac across the genome, it is possible that this mark is important for establishing widespread chromatin organisation to facilitate gene expression programs. The requirement for HBO1 as an organiser of chromatin architecture is supported by time course analysis of *HBO1* deleted cell lines that show loss of other histone acetylation marks occurs secondary to loss of H3K14ac (Kueh et al., 2020). These observations suggest that loss of H3K14ac leads to a complex array of primary and secondary effects affecting multiple chromatin modifications across the chromatin landscape rather than HBO1 being directly responsible for the expression of a discrete set of target genes.

Our analysis of GO terms relating to genes differentially expressed in *Hbo1* deleted ECs provided some insights into the programs that H3K14ac regulates. Strikingly, we found that many of the upregulated GO terms were associated with immature vessel phenotypes and behaviour such as *blood vessel development*, *angiogenesis* and *vasculature development*. Therefore, although EC identity was specified normally, they were maintained in a more immature state. This finding is consistent with our hypothesis that HBO1 would be required when new expression programs are activated. We would predict that the genes that are affected are those regulated by factors that are sensitive to loss of H3K14ac. Our finding that the adult vasculature did not express H3K14ac suggests that HBO1-dependent H3K14ac is unlikely to be required for maintaining gene expression patterns. Rather, this supports the

proposed role for HBO1-dependent H3K14ac in organising chromatin architecture required for new gene expression programs to be established, such as during neonatal sprouting angiogenesis. The surprising finding that genes involved in pathways such as "*angiogenesis"* and "*blood vessel development"* were upregulated in the absence of *Hbo1*, despite a reduced angiogenesis phenotype is likely explained by a disturbance in the number of angiogenic tip cells and a migration defect. The outcome is more tip cells that highly express angiogenic genes but a failure to migrate and grow the vasculature normally.

Overall, our data suggests that HBO1 is necessary for widespread chromatin organisation through its acetylation activity at H3K14 that enables ECs to activate new gene expression programs. This is important in settings such as during vessel maturation and tip cell directed normal and pathological vessel growth but is redundant in settings of vascular quiescence. scRNA-sequencing highlighted the pathways that are dependent upon the activity of H3K14ac and suggested that tip cells are the default cell type formed when this transcriptional organisation is disrupted.

Materials and Methods

Mice

Conditional *Hbo1* mice (Kueh et al., 2011), *Cdh5(PAC)-creER*^{T2} mice (Wang et al., 2010) and *ROSA26*$^{Sortm4(ACTB-tdTomato,-EGFP)Luo}$ (*mTmG*) (Muzumdar et al., 2007) have all been previously described. Animals were maintained on an inbred C57BL/6 background. The day of birth was termed P0. Mice of both sexes were used. To induce *Cdh5(PAC)-creER*^{T2}, mice were injected with 50 µg tamoxifen (MP Biomedicals, dissolved in sterile corn oil (Sigma, #C8267) plus 5% ethanol) by intragastric injection at postnatal day 1 (P1) and P2 using 0.3 mL syringe with attached 29G needle (BD #326103). 6-week-old adult mice were treated by oral gavage with 150 mg/kg tamoxifen prepared as above for three consecutive days and analysed at 10 weeks. Control mice were the following genotypes: *Hbo1*$^{fl/+}$*;Cdh5(PAC)-creER*$^{T2+}$ (heterozygote following tamoxifen administration), *Hbo1*$^{fl/+}$ and *Hbo1*$^{fl/fl}$.

Oxygen-induced retinopathy

Nursing dams with P7 pups were housed in a Perspex chamber (BioSpherix) and exposed continuously to 74±1% oxygen in air maintained by a ProOx110 oxygen controller (BioSpherix). Exposure to high oxygen was from P7 – P12 before returning to normal room air (~20% oxygen). Pups were fostered to BALB/c females following exposure to three days of high oxygen to prevent oxygen toxicity in dams. Neovascularisation was assessed at P17.

Immunohistochemical staining

For whole-mount immunohistochemistry, eyes were fixed for 2 h in 4% paraformaldehyde at 4^{O}C before dissecting and blocking retinas for 1 h at room temperature in Dulbecco's phosphate buffered saline (DPBS) with 1% Triton X-100 and 2% donkey serum. Retinas were stained with primary antibodies prepared in blocking solution overnight at 4˚C, washed in DPBS containing 0.01% Triton X-100, then stained overnight with secondary antibodies prepared in blocking solution. Primary antibodies were rat anti-PECAM1/CD31 (BD Pharmingen, 553370, 1/100), goat anti-PECAM1/CD31 (R&D Systems, AF3628, 1/200), rabbit anti-H3K14ac (Millipore, 07-353, 1/500), goat anti-collagen IV (Merck, AB769, 1/100), rabbit anti-cleaved (active) caspase 3 (CST, 9664, 1/50), rat anti-VE cadherin (BD Pharmingen, 555289, 1/500), rabbit anti-FLI1 (Abcam, ab15289, 1/200), human anti-ANG2 (4H10, 1/200) (Han et al., 2016), goat anti-ESM1 (R&D Systems, AF1999, 1/100), goat anti-DLL4 (R&D Systems, AF1389, 1/100), rabbit anti-EGFP (Invitrogen, A11122, 1/500), and rabbit anti-GM130 conjugated to A647 (Abcam, ab195303, 1/500). Secondary antibodies were donkey anti-rabbit-Cy3 (Jackson, 711-165-152), donkey anti-rabbit-AF647 (Jackson, 711-605-152, donkey anti-rat-DL488 (Jackson, 712-485-153), donkey anti-rat-Cy3 (Jackson, 712-165-150), donkey anti-rat-AF647 (Jackson, 712-605-150), donkey anti-goat-DL405 (Jackson, 705-475-147) and donkey anti-goat-Cy3 (Jackson, 705-165-147). All secondary antibodies used at 1/400. Retinas were incubated in 2 µg/ml Hoechst 33342 (Invitrogen, H3570) in 0.01% Triton-X 100 DPBS for 2 hours at room temperature and imaged same day. Retinas were mounted with Prolong Diamond (Invitrogen, P36961). 5-ethynyl-2'-deoxyuridine (EdU) was dissolved in DMSO to a concentration of 10 mg/ml. P6 pups were administered 100 µg EdU diluted in DPBS by intra-peritoneal injection using 0.3 mL syringe with attached 29G needle (BD #326103). Cells were labelled with EdU for 2 hours before euthanising mouse. Eyes were dissected and stained as per procedure above. Click-iT EdU Alexa Fluor 647 (Invitrogen #C10340) was performed as per manufacturer's instructions prior to mounting retina onto glass slide.

Imaging & image analysis

Retinas were imaged using a Leica TCS SP8 confocal microscope using 10x/0.4 NA, 20x/0.75 NA or 40x/1.30 NA objectives and Leica Application Suite software. All image analysis was performed in the FIJI distribution of ImageJ software (Schindelin et al., 2012). H3K14ac expression was analysed as the mean pixel intensity within endothelial nuclei, identified by Hoechst-33342 staining within PECAM1 signal using individual Z-slices. Entire EC nuclei were traced manually using freehand selection tool analysing >30 EC nuclei per image. H3K14ac levels in ECs were normalised to mean H3K14ac expression in >30 non-EC nuclei (determined as being PECAM1 negative). Vessel area was calculated using PECAM1 signal from maximum intensity projection images following application of a median filter (2 pixels) and 'despeckle' filter prior to manually adjusting threshold and measuring area. Radial outgrowth was quantified as mean distance from optic nerve head at centre of retina to edge of vasculature. Branch points and segment density were counted within two regions per retina from maximum projection collagen IV images (P6 retinas) and PECAM1 (adult retinas). P6 regions contained some arterial and venous plexus as well as some of the sprouting front plexus and adult regions were from near an artery in the peripheral retina. These images were despeckled, a 2 pixel median filter applied and made binary by thresholding area. The images were then skeletonised and the skeleton was analysed. Results output included details of number of junctions (branch points) as well as number of segments. These results were normalised to the area of the cropped region analysed. Proportion of retina vascularised by superficial and deep vessel layers was calculated by manually tracing around vascularised retina and normalised to manually traced total retina area. Apoptotic ECs (defined as cleaved (active) caspase 3^{+}/PECAM1^{+} cells enclosed by collagen IV signal) were quantified manually from confocal z stack images. Vessel regression was determined as a ratio of PECAM1+ vessel segment length to collagen IV+ vessel segment length. Binary masks of both PECAM1 and collagen IV channel were made by various morphological filters and thresholding signal manually. Collagen IV^{+} PECAM1^{-} vessel segment mask (ie. regressing vessels) was generated by subtracting PECAM1 mask from collagen IV mask. Collagen IV^{+} PECAM1^{-} mask and collagen IV mask were then skeletonised and length of vessels within each mask was measured. Collagen IV^{+} PECAM1^{-} : collagen IV ratio was generated automatically based on vessel length. Data was represented as PECAM1 : collagen IV ratio. Vessel regression was measured in multiple regions across the retina, including areas of the high-density sprouting front and less dense remodelling vessels. Proliferation was determined by labelling cells with EdU and quantified from maximum projection retina

overview images with optic nerve head area removed. Analysis was automated and generated binary masks of PECAM1, FLI1 and EdU signals using automatic thresholding and various morphological filters. The output generated total EC number across retina (defined as PECAM1+ FLI1+) as well as total proliferating cells across the retina. The number of proliferating ECs was calculated as PECAM1+ FLI1+ EdU+. ESM1+ ECs were quantified by drawing a line along the P6 sprouting front and manually counting ESM1+FLI1+PECAM1+ cells within 150 µm of this line. To distinguish ESM1+ ECs, individual Z-slices were examined. ESM1+ cells were normalised to total length of retina analysed. ESM1 expression was measured in individual ECs by segmenting the vasculature into individual cells using PECAM1 and FLI1 masks and then determining ESM1 positive and negative ECs by manually thresholding the ESM1 signal. Following this the mean level of ESM1 signal in ESM1 positive and negative cells was measured. Data is presented as mean ESM1 signal in ESM1 positive cells divided by mean ESM1 signal in ESM1 negative cells (background). ANG2+ ECs were quantified in a similar manner, instead using Hoechst 33342 as a nuclear maker to distinguish ECs. Vessel sprouts were defined as filopodia rich EC-body projections that extended from the edge of the vasculature and were counted manually along the sprouting front in one half of the retina and normalised to total length of retina analysed. To measure tip cell front-rear polarity, Golgi apparatus were visualised using GM130 and the orientation was analysed in ESM1+ ECs along the sprouting front in one half of the retina. The following criteria were used to assign Golgi apparatus orientation: (1) Golgi apparatus were defined as front polarised if part of the Golgi apparatus was between the sprouting edge and nucleus, (2) Golgi apparatus were defined as rear polarised if part of the Golgi apparatus was at the opposite side of nucleus to sprouting edge and (3) Golgi apparatus were defined as middle polarised if Golgi was neither front nor rear polarised or if Golgi apparatus was both front and rear polarised. Golgi apparatus orientation was represented as percentage in each position. For EC density and vessel width analysis, the number of FLI1+ ECs in each region were manually counted and normalised to vessel area for EC density analysis or to total vessel length for vessel width analysis. Total length of vessels was calculated by skeletonising the filtered PECAM1 signal and summing all vessel segments together. In the sprouting front this was measured in two regions at the edge of vessel plexus around the end of a vein and an artery. In the remodelling zone this was measured in two regions between an artery and vein. Neovascular and vaso-obliterated area were quantified based on collagen IV and PECAM1 signals, respectively, which were segmented manually in Adobe Photoshop CC 2015 and area calculated in FIJI. Neovascular area per retina was

normalised to total retina area. Where necessary, a despeckle filter was applied to select channels in images displayed in Fig.s for clarity. All data are shown as mean ± standard error of the mean (SEM). Statistical analyses were performed for all quantitative data by using Prism 7.0 (Graph Pad).

Quantitative real-time PCR on lung endothelial cells

P6 lungs were removed, cut into smaller pieces and dissociated using 0.26 WU/ml Liberase TM (Roche, #05401119001), 10 µg/ml DNase 1 (Worthington, #LS002139) in DPBS at 37˚C for 40 min at 800 rpm. Samples washed with 2% FCS in KDS-BSS salt solution and filtered through 70 µm filter mesh cap (Falcon). To deplete red blood cells, samples were incubated with rat anti-TER119 (BD Pharmingen, #553671) antibody for 20 min at 4˚C. Cell number in each sample were automatically counted using Countess cell counter (Invitrogen) and Dynabeads (Invitrogen, #11035) were added at a ratio of 1 bead : 1 cell and incubated with cells for 20 min at 4˚C. Red blood cells were depleted by applying sample to magnet and transferring supernatant to new tube. Depleted samples were stained using anti-PECAM1-APC (eBioscience #17-0311), anti-ICAM2-FITC (BD Pharmingen #557444) and anti-CD45-PerCPCy5.5 (BD Pharmingen #552950). ECs were sorted using ARIA IIu sorter (BD Bioscience) twice. ECs were defined as $PECAM1^{hi}ICAM2^{+}CD45.2^{-}$. Dead cells were excluded based on DAPI uptake. The first sort was using 'yield' parameter with the collected sample spun down and resorted using '4-way purity' parameter. ECs were pelleted and frozen. RNA was isolated using Qiagen RNeasy Microkit (Qiagen, #74004) according to manufacturer's instructions and quantified using Agilent Tapestation 2200. cDNA was synthesised using SuperScript II reverse transcriptase (Invitrogen). Real-time PCR was performed in triplicate using SensiMix SYBR Hi-ROX (Bioline, QT605-05) based detection on a LightCycler 480 (Roche). *Hbo1* gene expression was normalised to expression of *Hsp90*.

Single-cell RNA-sequencing (scRNA-seq) of retinal endothelial cells

Single-cell RNA-sequencing was performed on ECs isolated from P6 retinas of pairs of littermate control and $Hbo1^{iEC/iEC}$ mice. Control genotype mice were $Hbo1^{fl/+}Cdh5\text{-}creER^{T2+}$. Retinal ECs from four $Hbo1^{iEC/IEC}$ mice and four control mice were sorted into 384-well plates, sequenced and analysed, with one control mouse used across two plates, hence Fig. S3a and Fig. 4b shows five control samples. For all other analysis, the ECs from the control mouse on two plates were pooled and analysed as one sample. To ease in isolating ECs from the retina, the *mTmG* allele was intercrossed with control and $Hbo1^{iEC/iEC}$ mice. Both retinas

per animal were dissected and dissociated using 0.26 WU/ml Liberase TM, 10 µg/ml DNase 1 in DPBS at 37˚C for 30 min at 800 rpm. Samples were washed with 2% FCS in KDS-BSS salt solution and filtered through 50 µm filter mesh (Sefar, #03-50/31) into 4 ml tube and pelleted. Neural retinal cells were depleted by incubating with rat anti-CD24 (Biolegend, #101803, clone M1/69) and rat anti-CD73 (Biolegend, #127203, clone TY/11.8) antibodies for 20 min at 4˚C. Samples were then incubated with 25 µl of Dynabeads Biotin Binder beads (Invitrogen, #11047) for 20 min at 4˚C and depleted by applying sample to magnet and transferring supernatant to new tube. Depleted samples were stained with anti-PECAM1-PECy7 (eBioscience, #25-0311-82, clone 390) for 20 min on ice. Single ECs were flow sorted into a chilled 384-well PCR plate (Greiner, 785290) containing 1.2 µl of primer/lysis mix [20 nM indexed polydT primer (custom made, IDT), 1:6.000.000 dilution of ERCC RNA spike-in mix (Ambion, 4456740), 1 mM dNTPs (NEB, N0446S), 1.2 units SUPERaseIN Rnase Inhibitor (Thermo Fisher, AM2696), DEPC water (Thermo Fisher, AM9920)] using a BD FACSAria III flow cytometer (BD Biosciences, San Jose, CA, USA). Prepared RNA mixture plates were sealed and stored at -80˚C. ECs were defined as PECAM1^{hi}EGFP^{+}. Dead cells were excluded based on DAPI uptake. Between 171 and 185 single cells per animal were sorted. Excepting one plate that contained only control genotype ECs, all other plates contained ECs from pairs of littermate control and *Hbo1*$^{iEC/iEC}$ retinas. In total, five plates were collected, processed for sequencing and downstream analysis. Single cell transcriptome libraries were generated using the CelSeq2 protocol (Hashimshony et al., 2016) with the following adaptations: Second strand synthesis was performed using NEBNext Second Strand Synthesis module (NEB, #E6111S) in a final reaction volume of 8 µl and NucleoMag NGS Clean-up and Size select magnetic beads (Macherey-Nagel, 7449970.5) were used for all DNA purification and size selection steps. The libraries were sequenced on an Illumina NextSeq500 sequencer using an Illumina 75-cycle sequencing kit (sequencing run set-up: Read 1 – 14bp, Index read – 6 bp, Read 2 – 72 bp).

scRNA-seq analysis

CelSeq2 scRNA-sequencing reads were mapped to the GRCm38.p6 mouse genome and ERCC spike-in sequences using the Subread aligner (v2.2.4) (Liao et al., 2013)and assigned to genes using scPipe (v1.10.0) with GENCODE vM18 primary assembly annotation. Gene counts were exported as a matrix by scPipe with UMI-aware counting. All subsequent analysis was performed in R (version 4.0.0) (Team, 2020) with Bioconductor (version 3.11) (Huber et al., 2015) and was adapted from 'Orchestrating Single Cell Analysis with R'

(Amezquita et al., 2020). Due to differences in quality control (QC) metrics by plate, outlier thresholds were calculated per plate. Cells were removed from further analysis if they failed to achieve QC cutoffs as shown in Supp Table 6 for total read counts, total genes detected, percentage of reads from spike-in ERCC RNA and percentage of reads from mitochondrial genes. Overall 229 cells were excluded, leaving 1393 for downstream analysis. All genes detected in at least 1 sample were retained for downstream analysis (33,655 genes). Size factors were estimated using the normalization by deconvolution method (Lun et al., 2016a), as implemented in the scran package (v1.16.0), and used to compute log-transformed normalized expression values (logcounts). We estimated the per-gene 'biological' variation as the total variation minus an estimate of the 'technical' variation (estimated by fitting a plate-specific, mean-dependent trend to the variance of the spike-in transcripts). All genes with positive 'biological' variation that were not annotated as pseudogenes, ribosomal protein genes, genes on the sex chromosomes, or mitochondrial genes were declared as HVGs. We then performed principal component analysis (PCA) of the logcounts of the HVGs and performed further dimensionality reduction for the purposes of visualization using the uniform manifold approximation and projection (UMAP) method (McInnes et al., 2018). These principal components were used to build a shared nearest neighbour graph (Xu and Su, 2015) that was itself used as input to the Louvain algorithm, as implemented in the igraph package (v1.2.5) (Csardi and Nepusz, 2006), to identify clusters of similar cells. We next corrected for plate-specific differences using the mutual nearest neighbours (MNN) method (Haghverdi et al., 2018) as implemented in the batchelor package (v1.4.0). The MNN-corrected data were used in place of the principal components and data were re-clustered and visualized by UMAP. Clusters with highly similar expression patterns and assumed to underlie the same EC phenotype were merged in the same cluster. Next, we identified top-ranking marker genes for each cluster by performing pairwise differential gene expression analysis for each cluster against all other clusters using a Welch t-test. The results were ordered based on the overall $\log_2$ fold change, with the highest $\log_2$ fold change representing cluster specific markers. We used previously published known markers of EC phenotypes as indicated in text and other single-cell endothelial transcriptomic analysis (Vanlandewijck et al., 2018, Kalucka et al., 2020, Goveia et al., 2020) to annotate the clusters we identified based on their top-ranking marker gene expression. Annotation of proliferating clusters was performed using the prediction method implemented in the 'cyclone' function from the scran package (v1.16.0) (Scialdone et al., 2015). To perform differential expression analyses we

first created pseudobulk samples by summing the single-cell counts from the same sample and, optionally, cluster (Lun and Marioni, 2017, Crowell et al., 2020). These pseudobulk samples were used as input for differential expression analyses using the quasi-likelihood methods from the edgeR package (v3.30.3) (Chen et al., 2016, Lun et al., 2016b). Heatmaps were generated on the pseudobulk logCPM values using the pheatmap package (v1.0.12) with row normalisation. Gene Ontology (GO) term and KEGG pathway analysis were performed using 'goana' and 'kegga' functions from the *limma* package (Ritchie et al., 2015). Comparison of differentially expressed genes to other pathways involved in sprouting angiogenesis was assessed by rotation gene set testing using the 'fry' function from edgeR and visualized by barcode plots. Significance indicated by two-sided p-value for testing where the set is differentially expressed, as a whole, is either up or down. Differential abundance analysis was performed on samples normalised for total number of cells using the *edgeR* package. Single cell RNA-seq data are available through the Gene Expression Omnibus under accession number #: GSE161893

Chromatin immunoprecipitation and sequencing (ChIP-seq)

HUVEC (Lonza, #C2519A) were grown in 15 cm^2 dishes with EGM-2 media (Lonza, #CC-3162) under hypoxic (3%) conditions. Each 15 cm^2 dish was considered 2x IP preps. 90-100% confluent HUVEC were stimulated with 25 ng/ml $VEGF_{165}$ (Peprotech, #100-20) for 2 hours, then fixed with 1% methanol-free formaldehyde for 10 min at RT and quenched with 0.125M glycine. Fixed cells were scraped with DPBS, transferred to a tube and pelleted at 400 g for 5 min at 4˚C. Cells were lysed using 1x Buffer A (CST #14282S) supplemented with sodium butyrate, protease inhibitors and DTT on ice for 15 min. Nuclei were pelleted at 1500 g for 5 min at 4˚C and resuspended in 1x Buffer B (CST #14282S) supplemented with sodium butyrate, protease inhibitors and DTT. Resuspended nuclei were passed through 100 µm filter mesh and centrifuged at 1500 g for 5 min at 4˚C. Nuclei were resuspended in 100 µl supplemented Buffer B per IP prep and transferred to 1 ml tube. Chromatin was fragmented to between 150 bp and 900 bp using 0.15 µl micrococcal nuclease (CST #10011) per IP prep for 20 min at 37˚C. Digest was stopped by adding 10 µl of 0.5 M EDTA per IP prep and placed on ice. Nuclei were pelleted at 16000 g for 1 min at 4˚C. Nuclear pellet was resuspended in 150 µl ChIP lysis buffer (50 mM Tris-HCl pH 8, 5 mM EDTA, 0.5% SDS, supplemented with protease inhibitors, sodium butyrate) per IP and incubated on ice for 10 min. Lysates were sonicated to total power of 60 J to break the nuclear membrane. Lysates

were cleared by centrifuging at 16000 g for 10 min at 4˚C and supernatant transferred to new tube. Concentration was determined using A280 Nanodrop reading. 40 µg chromatin was used per H3K14ac and panH3 IP and 80 µg chromatin was used per IgG IP. Samples were diluted 1/10 with ChIP dilution buffer (20 mM Tris-HCl pH 8, 2 mM EDTA, 150 mM NaCl, 0.01% SDS, 1% Triton X-100 and supplemented with protease inhibitors, sodium butyrate) in DNA LoBind tubes (Eppendorf #0030108035). 2% of volume removed as input sample. Each IP prep was incubated with 15 µl Magna ChIP A+G beads (Merck, #16-663) for 1 hour at 4˚C to and applied to magnet to remove non-specific binding. Supernatant was transferred to new LoBind tube and incubated overnight at 4˚C with either rabbit anti-H3K14ac (Abcam, ab52946, 5 µg per IP), mouse anti-pan H3 (Abcam, ab10799, 10 µg per IP) and rabbit anti-IgG (Abcam, ab172730, 10 µg per IP) antibodies. Samples were incubated with 15 µl pre-washed Magna ChIP A+G beads for 1 hour at 4˚C. Beads were washed three times with TSEI buffer (20 mM Tris-HCl pH 8, 2 mM EDTA, 150 mM NaCl, 0.1% SDS, 1% Triton X-100), once with TSEII buffer (20 mM Tris-HCl pH 8, 2 mM EDTA, 500 mM NaCl, 0.1% SDS, 1% Triton X-100), TSEIII buffer (10 mM Tris-HCl pH 8, 1 mM EDTA, 250 mM LiCl, 0.1% SDS, 1% sodium deoxycholate, 1% IGEPAL CA-630) and TE buffer (10 mM Tris-HCl pH 8, 1 mM EDTA). Chromatin was eluted by incubating beads with 75 µl ChIP elution buffer (1% SDS, 0.1 M $NaHCO_3$) for 30 min at 65˚C 1000 rpm, applying to magnet and transferring to new LoBind tube. Samples (including input) were reverse crosslinked with 20 µg RNase A at 37˚C for 30 min and then 40 µg Proteinase K at 65˚C overnight. DNA was purified using Qiagen MinElute PCR Purification Kit (Qiagen, #28004) following manufacturer's instructions. DNA concentration was determined by Agilent Tapestation 2200. 5 ng of DNA per three H3K14ac, two panH3 and two input samples were used for sequencing library preparation and generated using an Illumina TruSeq DNA library prep kit. ChIP libraries were sequenced on an Illumina NextSeq 500 sequencer. H3K14ac samples were sequenced with twice the depth as pan H3 and input samples, by loading more starting material.

ChIP-seq analysis

ChIP-seq reads were aligned to hg38 using Rsubread (Liao et al., 2019). The ChIP-Seq libraries were GC corrected using Benjamini's and Speed's method implemented by the deepTools program (Ramirez et al., 2016). The genomic features - Gene bodies, Pseudogene bodies, TSS - 1 kb to TSS + 1 kb regions, TSS - 2 kb to TSS regions, TES to TES + 2 kb regions, and Intergenic regions defined as ≥10 kb away from any gene excluding blacklisted regions - were considered in the analysis using hg38 NCBI annotation. The number of read

pairs overlapping each genomic region was summarized using featureCounts. Student's T-Test was used to compare log2 counts per million (CPM) between the non-overlapping genomic regions. Differential expression (DE) analysis between H3K14ac and pan H3 with respect to each of the genomic regions were undertaken using the edgeR and limma (Ritchie et al., 2015) software packages. Library sizes were normalized using the trimmed mean of M-values (TMM) method (Robinson and Oshlack, 2010). Differential expression was assessed using glmQLFit (quasi-likelihood generalised linear models) in edgeR (Chen et al., 2016). Over-representation of Gene Ontology (GO) terms for the differentially expressed genes was identified using limma's goana function. Barcode plots illustrating the enrichment of gene sets in H3K14ac compared to pan H3 were drawn using limma's barcodeplot function. Gene set enrichment tests used the roast method (Wu et al., 2010). The coverages for non-overlapping 5 bp bins for each ChIP-seq library were computed using the deepTools program. ChIP-seq data are available through the Gene Expression Omnibus under accession number #: GSE161893

Study approval

All experiments involving animals were performed with procedures approved by The Walter & Eliza Hall Institute of Medical Research Animal Ethics Committee.

Author Contributions

Z.L.G. performed experiments, analysed data & wrote the manuscript; P.F.H., analysed single-cell RNA-sequencing data, W.A. & A.L.G., analysed ChIP-sequencing data; L.W. developed image analysis tools; S.M.L. & T.M.B. performed experiments; D.A.Z., G.K.S. supervised research; T.T. & R.C.A.S. provided essential equipment, A.K.V. & L.C. conceived the project, supervised research, analysed data & wrote the manuscript. All authors contributed to and approved the manuscript.

Acknowledgements

The authors thank Ralf H. Adams (Max Planck Institute, Münster) for Cdh5(PAC)-creERT2 mice, Goh Young Koh (KAIST, Daejeon) for generously providing the anti-ANG2 antibody 4H10, Glenna-Faye Dabrowski, Lauren Wilkens, Andrea Briffa, Jaclyn Gilbert and Dannielle Cooper for expert animal care, and members of the Epigenetics and Development Division (Walter & Eliza Hall Institute) for informative discussion. This work was made

possible through Victorian State Government Operational Infrastructure Support and Australian Government NHMRC IRIISS. This work was supported by the National Health and Medical Research Council, Australia through Project Grants 1084248 and 1143612 to A.K.V. and T.T., Research Fellowships 1081421 to A.K.V. and 1003435 to T.T., Investigator Grant 1176789 to A.K.V.; the Australian Research Council (Future Fellowships: 110100891 to L.C.); the L.E.W Carty Charitable Fund (to L.C.); Australian Government Research Training Program Scholarship (to Z.L.G.); the RMH Neuroscience Foundation (to R.C.A.S).

Competing Interests

The authors have declared that no conflict of interest exists.

References

AIELLO, L. P., PIERCE, E. A., FOLEY, E. D., TAKAGI, H., CHEN, H., RIDDLE, L., FERRARA, N., KING, G. L. & SMITH, L. E. 1995. Suppression of retinal neovascularization in vivo by inhibition of vascular endothelial growth factor (VEGF) using soluble VEGF-receptor chimeric proteins. *Proc Natl Acad Sci U S A,* 92**,** 10457-61.

AMEZQUITA, R. A., LUN, A. T. L., BECHT, E., CAREY, V. J., CARPP, L. N., GEISTLINGER, L., MARINI, F., RUE-ALBRECHT, K., RISSO, D., SONESON, C., WALDRON, L., PAGES, H., SMITH, M. L., HUBER, W., MORGAN, M., GOTTARDO, R. & HICKS, S. C. 2020. Orchestrating single-cell analysis with Bioconductor. *Nat Methods,* 17**,** 137-145.

ARIMA, S., NISHIYAMA, K., KO, T., ARIMA, Y., HAKOZAKI, Y., SUGIHARA, K., KOSEKI, H., UCHIJIMA, Y., KURIHARA, Y. & KURIHARA, H. 2011. Angiogenic morphogenesis driven by dynamic and heterogeneous collective endothelial cell movement. *Development,* 138**,** 4763-76.

AVVAKUMOV, N., LALONDE, M. E., SAKSOUK, N., PAQUET, E., GLASS, K. C., LANDRY, A. J., DOYON, Y., CAYROU, C., ROBITAILLE, G. A., RICHARD, D. E., YANG, X. J., KUTATELADZE, T. G. & COTE, J. 2012. Conserved molecular interactions within the HBO1 acetyltransferase complexes regulate cell proliferation. *Mol Cell Biol,* 32**,** 689-703.

BENTLEY, K., FRANCO, C. A., PHILIPPIDES, A., BLANCO, R., DIERKES, M., GEBALA, V., STANCHI, F., JONES, M., ASPALTER, I. M., CAGNA, G., WESTROM, S., CLAESSON-WELSH, L., VESTWEBER, D. & GERHARDT, H. 2014. The role of differential VE-cadherin dynamics in cell rearrangement during angiogenesis. *Nat Cell Biol,* 16**,** 309-21.

CHEN, Y., LUN, A. T. & SMYTH, G. K. 2016. From reads to genes to pathways: differential expression analysis of RNA-Seq experiments using Rsubread and the edgeR quasi-likelihood pipeline. *F1000Res,* 5**,** 1438.

CRIST, A. M., YOUNG, C. & MEADOWS, S. M. 2017. Characterization of arteriovenous identity in the developing neonate mouse retina. *Gene Expr Patterns,* 23-24**,** 22-31.

CROWELL, H. L., SONESON, C., GERMAIN, P., CALINI, D., COLLIN, L., RAPOSO, C., MALHOTRA, D. & ROBINSON, M. D. 2020. On the discovery of subpopulation-specific state transitions from multi-saome multi-condition single-cell RNA sequencing data. *BioRxiv,* 713412.

CSARDI, G. & NEPUSZ, T. 2006. The igraph software package for complex network research. *InterJournal,* Complex Systems http://igraph.org.

DALLINGA, M. G., HABANI, Y. I., KAYSER, R. P., VAN NOORDEN, C. J. F., KLAASSEN, I. & SCHLINGEMANN, R. O. 2020. IGF-binding proteins 3 and 4 are regulators of sprouting angiogenesis. *Mol Biol Rep,* 47**,** 2561-2572.

DEL TORO, R., PRAHST, C., MATHIVET, T., SIEGFRIED, G., KAMINKER, J. S., LARRIVEE, B., BREANT, C., DUARTE, A., TAKAKURA, N., FUKAMIZU, A., PENNINGER, J. & EICHMANN, A. 2010. Identification and functional analysis of endothelial tip cell-enriched genes. *Blood,* 116**,** 4025-33.

DUAN, B., YE, D., ZHU, S., JIA, W., LU, C., WANG, G., GUO, X., YU, Y., WU, C. & KANG, J. 2017. HDAC10 promotes angiogenesis in endothelial cells through the PTPN22/ERK axis. *Oncotarget,* 8**,** 61338-61349.

DUBRAC, A., GENET, G., OLA, R., ZHANG, F., PIBOUIN-FRAGNER, L., HAN, J., ZHANG, J., THOMAS, J. L., CHEDOTAL, A., SCHWARTZ, M. A. & EICHMANN, A. 2016. Targeting NCK-Mediated Endothelial Cell Front-Rear Polarity Inhibits Neovascularization. *Circulation,* 133**,** 409-21.

EHLING, M., ADAMS, S., BENEDITO, R. & ADAMS, R. H. 2013. Notch controls retinal blood vessel maturation and quiescence. *Development,* 140**,** 3051-61.

FANG, J. S., COON, B. G., GILLIS, N., CHEN, Z., QIU, J., CHITTENDEN, T. W., BURT, J. M., SCHWARTZ, M. A. & HIRSCHI, K. K. 2017. Shear-induced Notch-Cx37-p27

axis arrests endothelial cell cycle to enable arterial specification. *Nat Commun,* 8**,** 2149.

FELLER, C., FORNE, I., IMHOF, A. & BECKER, P. B. 2015. Global and specific responses of the histone acetylome to systematic perturbation. *Mol Cell,* 57**,** 559-71.

FERRARA, N. & ADAMIS, A. P. 2016. Ten years of anti-vascular endothelial growth factor therapy. *Nat Rev Drug Discov,* 15**,** 385-403.

FRANCO, C. A., JONES, M. L., BERNABEU, M. O., GEUDENS, I., MATHIVET, T., ROSA, A., LOPES, F. M., LIMA, A. P., RAGAB, A., COLLINS, R. T., PHNG, L. K., COVENEY, P. V. & GERHARDT, H. 2015. Dynamic endothelial cell rearrangements drive developmental vessel regression. *PLoS Biol,* 13**,** e1002125.

GERHARDT, H., GOLDING, M., FRUTTIGER, M., RUHRBERG, C., LUNDKVIST, A., ABRAMSSON, A., JELTSCH, M., MITCHELL, C., ALITALO, K., SHIMA, D. & BETSHOLTZ, C. 2003. VEGF guides angiogenic sprouting utilizing endothelial tip cell filopodia. *J Cell Biol,* 161**,** 1163-77.

GEUDENS, I. & GERHARDT, H. 2011. Coordinating cell behaviour during blood vessel formation. *Development,* 138**,** 4569-83.

GOVEIA, J., ROHLENOVA, K., TAVERNA, F., TREPS, L., CONRADI, L. C., PIRCHER, A., GELDHOF, V., DE ROOIJ, L., KALUCKA, J., SOKOL, L., GARCIA-CABALLERO, M., ZHENG, Y., QIAN, J., TEUWEN, L. A., KHAN, S., BOECKX, B., WAUTERS, E., DECALUWE, H., DE LEYN, P., VANSTEENKISTE, J., WEYNAND, B., SAGAERT, X., VERBEKEN, E., WOLTHUIS, A., TOPAL, B., EVERAERTS, W., BOHNENBERGER, H., EMMERT, A., PANOVSKA, D., DE SMET, F., STAAL, F. J. T., MCLAUGHLIN, R. J., IMPENS, F., LAGANI, V., VINCKIER, S., MAZZONE, M., SCHOONJANS, L., DEWERCHIN, M., EELEN, G., KARAKACH, T. K., YANG, H., WANG, J., BOLUND, L., LIN, L., THIENPONT, B., LI, X., LAMBRECHTS, D., LUO, Y. & CARMELIET, P. 2020. An Integrated Gene Expression Landscape Profiling Approach to Identify Lung Tumor Endothelial Cell Heterogeneity and Angiogenic Candidates. *Cancer Cell,* 37**,** 21-36 e13.

GRANT, Z. L., WHITEHEAD, L., WONG, V. H., HE, Z., YAN, R. Y., MILES, A. R., BENEST, A. V., BATES, D. O., PRAHST, C., BENTLEY, K., BUI, B. V., SYMONS, R. C. & COULTAS, L. 2020. Blocking endothelial apoptosis revascularizes the retina in a model of ischemic retinopathy. *J Clin Invest*.

HAGHVERDI, L., LUN, A. T. L., MORGAN, M. D. & MARIONI, J. C. 2018. Batch effects in single-cell RNA-sequencing data are corrected by matching mutual nearest neighbors. *Nat Biotechnol,* 36**,** 421-427.

HAN, S., LEE, S. J., KIM, K. E., LEE, H. S., OH, N., PARK, I., KO, E., OH, S. J., LEE, Y. S., KIM, D., LEE, S., LEE, D. H., LEE, K. H., CHAE, S. Y., LEE, J. H., KIM, S. J., KIM, H. C., KIM, S., KIM, S. H., KIM, C., NAKAOKA, Y., HE, Y., AUGUSTIN, H. G., HU, J., SONG, P. H., KIM, Y. I., KIM, P., KIM, I. & KOH, G. Y. 2016. Amelioration of sepsis by TIE2 activation-induced vascular protection. *Sci Transl Med,* 8**,** 335ra55.

HANSEN, B. K., GUPTA, R., BALDUS, L., LYON, D., NARITA, T., LAMMERS, M., CHOUDHARY, C. & WEINERT, B. T. 2019. Analysis of human acetylation stoichiometry defines mechanistic constraints on protein regulation. *Nat Commun,* 10**,** 1055.

HASAN, S. S., TSARYK, R., LANGE, M., WISNIEWSKI, L., MOORE, J. C., LAWSON, N. D., WOJCIECHOWSKA, K., SCHNITTLER, H. & SIEKMANN, A. F. 2017. Endothelial Notch signalling limits angiogenesis via control of artery formation. *Nat Cell Biol,* 19**,** 928-940.

HASHIMSHONY, T., SENDEROVICH, N., AVITAL, G., KLOCHENDLER, A., DE LEEUW, Y., ANAVY, L., GENNERT, D., LI, S., LIVAK, K. J., ROZENBLATT-ROSEN, O., DOR, Y., REGEV, A. & YANAI, I. 2016. CEL-Seq2: sensitive highly-multiplexed single-cell RNA-Seq. *Genome Biol,* 17**,** 77.

HUBER, W., CAREY, V. J., GENTLEMAN, R., ANDERS, S., CARLSON, M., CARVALHO, B. S., BRAVO, H. C., DAVIS, S., GATTO, L., GIRKE, T., GOTTARDO, R., HAHNE, F., HANSEN, K. D., IRIZARRY, R. A., LAWRENCE, M., LOVE, M. I., MACDONALD, J., OBENCHAIN, V., OLES, A. K., PAGES, H., REYES, A., SHANNON, P., SMYTH, G. K., TENENBAUM, D., WALDRON, L. & MORGAN, M. 2015. Orchestrating high-throughput genomic analysis with Bioconductor. *Nat Methods,* 12**,** 115-21.

IIZUKA, M. & STILLMAN, B. 1999. Histone acetyltransferase HBO1 interacts with the ORC1 subunit of the human initiator protein. *J Biol Chem,* 274**,** 23027-34.

IZUMI, N., HELKER, C., EHLING, M., BEHRENS, A., HERZOG, W. & ADAMS, R. H. 2012. Fbxw7 controls angiogenesis by regulating endothelial Notch activity. *PLoS One,* 7**,** e41116.

JAKAB, M. & AUGUSTIN, H. G. 2020. Understanding angiodiversity: insights from single cell biology. *Development,* 147.

JAKOBSSON, L., FRANCO, C. A., BENTLEY, K., COLLINS, R. T., PONSIOEN, B., ASPALTER, I. M., ROSEWELL, I., BUSSE, M., THURSTON, G., MEDVINSKY, A., SCHULTE-MERKER, S. & GERHARDT, H. 2010. Endothelial cells dynamically compete for the tip cell position during angiogenic sprouting. *Nat Cell Biol,* 12**,** 943-53.

JEONG, H. W., HERNANDEZ-RODRIGUEZ, B., KIM, J., KIM, K. P., ENRIQUEZ-GASCA, R., YOON, J., ADAMS, S., SCHOLER, H. R., VAQUERIZAS, J. M. & ADAMS, R. H. 2017. Transcriptional regulation of endothelial cell behavior during sprouting angiogenesis. *Nat Commun,* 8**,** 726.

JOHMURA, Y., OSADA, S., NISHIZUKA, M. & IMAGAWA, M. 2008. FAD24 acts in concert with histone acetyltransferase HBO1 to promote adipogenesis by controlling DNA replication. *J Biol Chem,* 283**,** 2265-74.

KALUCKA, J., DE ROOIJ, L., GOVEIA, J., ROHLENOVA, K., DUMAS, S. J., META, E., CONCHINHA, N. V., TAVERNA, F., TEUWEN, L. A., VEYS, K., GARCIA-CABALLERO, M., KHAN, S., GELDHOF, V., SOKOL, L., CHEN, R., TREPS, L., BORRI, M., DE ZEEUW, P., DUBOIS, C., KARAKACH, T. K., FALKENBERG, K. D., PARYS, M., YIN, X., VINCKIER, S., DU, Y., FENTON, R. A., SCHOONJANS, L., DEWERCHIN, M., EELEN, G., THIENPONT, B., LIN, L., BOLUND, L., LI, X., LUO, Y. & CARMELIET, P. 2020. Single-Cell Transcriptome Atlas of Murine Endothelial Cells. *Cell,* 180**,** 764-779 e20.

KARMODIYA, K., KREBS, A. R., OULAD-ABDELGHANI, M., KIMURA, H. & TORA, L. 2012. H3K9 and H3K14 acetylation co-occur at many gene regulatory elements, while H3K14ac marks a subset of inactive inducible promoters in mouse embryonic stem cells. *BMC Genomics,* 13**,** 424.

KIM, Y. H., CHOI, J., YANG, M. J., HONG, S. P., LEE, C. K., KUBOTA, Y., LIM, D. S. & KOH, G. Y. 2019. A MST1-FOXO1 cascade establishes endothelial tip cell polarity and facilitates sprouting angiogenesis. *Nat Commun,* 10**,** 838.

KUCHARZEWSKA, P., WELCH, J. E., SVENSSON, K. J. & BELTING, M. 2010. Ornithine decarboxylase and extracellular polyamines regulate microvascular sprouting and actin cytoskeleton dynamics in endothelial cells. *Exp Cell Res,* 316**,** 2683-91.

KUEH, A. J., DIXON, M. P., VOSS, A. K. & THOMAS, T. 2011. HBO1 is required for H3K14 acetylation and normal transcriptional activity during embryonic development. *Mol Cell Biol,* 31**,** 845-60.

KUEH, A. J., ECCLES, S., TANG, L., GARNHAM, A. L., MAY, R. E., HEROLD, M. J., SMYTH, G. K., VOSS, A. K. & THOMAS, T. 2020. HBO1 (KAT7) Does Not Have an Essential Role in Cell Proliferation, DNA Replication, or Histone 4 Acetylation in Human Cells. *Mol Cell Biol,* 40.

LALONDE, M. E., AVVAKUMOV, N., GLASS, K. C., JONCAS, F. H., SAKSOUK, N., HOLLIDAY, M., PAQUET, E., YAN, K., TONG, Q., KLEIN, B. J., TAN, S., YANG, X. J., KUTATELADZE, T. G. & COTE, J. 2013. Exchange of associated factors directs a switch in HBO1 acetyltransferase histone tail specificity. *Genes Dev,* 27**,** 2009-24.

LARRIVEE, B., PRAHST, C., GORDON, E., DEL TORO, R., MATHIVET, T., DUARTE, A., SIMONS, M. & EICHMANN, A. 2012. ALK1 signaling inhibits angiogenesis by cooperating with the Notch pathway. *Dev Cell,* 22**,** 489-500.

LEE, J., KIM, K. E., CHOI, D. K., JANG, J. Y., JUNG, J. J., KIYONARI, H., SHIOI, G., CHANG, W., SUDA, T., MOCHIZUKI, N., NAKAOKA, Y., KOMURO, I., YOO, O. J. & KOH, G. Y. 2013. Angiopoietin-1 guides directional angiogenesis through integrin alphavbeta5 signaling for recovery of ischemic retinopathy. *Sci Transl Med,* 5**,** 203ra127.

LIAO, Y., SMYTH, G. K. & SHI, W. 2013. The Subread aligner: fast, accurate and scalable read mapping by seed-and-vote. *Nucleic Acids Res,* 41**,** e108.

LIAO, Y., SMYTH, G. K. & SHI, W. 2019. The R package Rsubread is easier, faster, cheaper and better for alignment and quantification of RNA sequencing reads. *Nucleic Acids Res,* 47**,** e47.

LUKOWSKI, S. W., PATEL, J., ANDERSEN, S. B., SIM, S. L., WONG, H. Y., TAY, J., WINKLER, I., POWELL, J. E. & KHOSROTEHRANI, K. 2019. Single-Cell Transcriptional Profiling of Aortic Endothelium Identifies a Hierarchy from Endovascular Progenitors to Differentiated Cells. *Cell Rep,* 27**,** 2748-2758 e3.

LUN, A. T., BACH, K. & MARIONI, J. C. 2016a. Pooling across cells to normalize single-cell RNA sequencing data with many zero counts. *Genome Biol,* 17**,** 75.

LUN, A. T., CHEN, Y. & SMYTH, G. K. 2016b. It's DE-licious: A Recipe for Differential Expression Analyses of RNA-seq Experiments Using Quasi-Likelihood Methods in edgeR. *Methods Mol Biol,* 1418**,** 391-416.

LUN, A. T. L. & MARIONI, J. C. 2017. Overcoming confounding plate effects in differential expression analyses of single-cell RNA-seq data. *Biostatistics,* 18**,** 451-464.

MCINNES, L., HEALY, J., SAUL, N. & GROSSBERGE, L. 2018. UMAP: Uniform Manifold Approximation and Projection. *Journal of Open Source Software,* 3**,** 361.

MILLER, J. W., LE COUTER, J., STRAUSS, E. C. & FERRARA, N. 2013. Vascular endothelial growth factor a in intraocular vascular disease. *Ophthalmology,* 120**,** 106-14.

MISHIMA, Y., MIYAGI, S., SARAYA, A., NEGISHI, M., ENDOH, M., ENDO, T. A., TOYODA, T., SHINGA, J., KATSUMOTO, T., CHIBA, T., YAMAGUCHI, N., KITABAYASHI, I., KOSEKI, H. & IWAMA, A. 2011. The Hbo1-Brd1/Brpf2 complex is responsible for global acetylation of H3K14 and required for fetal liver erythropoiesis. *Blood,* 118**,** 2443-53.

MOYA, I. M., UMANS, L., MAAS, E., PEREIRA, P. N., BEETS, K., FRANCIS, A., SENTS, W., ROBERTSON, E. J., MUMMERY, C. L., HUYLEBROECK, D. & ZWIJSEN, A. 2012. Stalk cell phenotype depends on integration of Notch and Smad1/5 signaling cascades. *Dev Cell,* 22**,** 501-14.

MUZUMDAR, M. D., TASIC, B., MIYAMICHI, K., LI, L. & LUO, L. 2007. A global double-fluorescent Cre reporter mouse. *Genesis,* 45**,** 593-605.

PEGG, A. E. 2006. Regulation of ornithine decarboxylase. *J Biol Chem,* 281**,** 14529-32.

PHNG, L. K., POTENTE, M., LESLIE, J. D., BABBAGE, J., NYQVIST, D., LOBOV, I., ONDR, J. K., RAO, S., LANG, R. A., THURSTON, G. & GERHARDT, H. 2009. Nrarp coordinates endothelial Notch and Wnt signaling to control vessel density in angiogenesis. *Dev Cell,* 16**,** 70-82.

PITULESCU, M. E., SCHMIDT, I., GIAIMO, B. D., ANTOINE, T., BERKENFELD, F., FERRANTE, F., PARK, H., EHLING, M., BILJES, D., ROCHA, S. F., LANGEN, U. H., STEHLING, M., NAGASAWA, T., FERRARA, N., BORGGREFE, T. & ADAMS, R. H. 2017. Dll4 and Notch signalling couples sprouting angiogenesis and artery formation. *Nat Cell Biol,* 19**,** 915-927.

POTENTE, M., GERHARDT, H. & CARMELIET, P. 2011. Basic and therapeutic aspects of angiogenesis. *Cell,* 146**,** 873-87.

POTENTE, M. & MAKINEN, T. 2017. Vascular heterogeneity and specialization in development and disease. *Nat Rev Mol Cell Biol,* 18**,** 477-494.

RAIMONDI, C., FANTIN, A., LAMPROPOULOU, A., DENTI, L., CHIKH, A. & RUHRBERG, C. 2014. Imatinib inhibits VEGF-independent angiogenesis by targeting neuropilin 1-dependent ABL1 activation in endothelial cells. *J Exp Med,* 211**,** 1167-83.

RAMA, N., DUBRAC, A., MATHIVET, T., NI CHARTHAIGH, R. A., GENET, G., CRISTOFARO, B., PIBOUIN-FRAGNER, L., MA, L., EICHMANN, A. & CHEDOTAL, A. 2015. Slit2 signaling through Robo1 and Robo2 is required for retinal neovascularization. *Nat Med,* 21**,** 483-91.

RAMIREZ, F., RYAN, D. P., GRUNING, B., BHARDWAJ, V., KILPERT, F., RICHTER, A. S., HEYNE, S., DUNDAR, F. & MANKE, T. 2016. deepTools2: a next generation web server for deep-sequencing data analysis. *Nucleic Acids Res,* 44**,** W160-5.

RITCHIE, M. E., PHIPSON, B., WU, D., HU, Y., LAW, C. W., SHI, W. & SMYTH, G. K. 2015. limma powers differential expression analyses for RNA-sequencing and microarray studies. *Nucleic Acids Res,* 43**,** e47.

ROBINSON, M. D. & OSHLACK, A. 2010. A scaling normalization method for differential expression analysis of RNA-seq data. *Genome Biol,* 11**,** R25.

ROCHA, S. F., SCHILLER, M., JING, D., LI, H., BUTZ, S., VESTWEBER, D., BILJES, D., DREXLER, H. C., NIEMINEN-KELHA, M., VAJKOCZY, P., ADAMS, S., BENEDITO, R. & ADAMS, R. H. 2014. Esm1 modulates endothelial tip cell behavior and vascular permeability by enhancing VEGF bioavailability. *Circ Res,* 115**,** 581-90.

SABBAGH, M. F., HENG, J. S., LUO, C., CASTANON, R. G., NERY, J. R., RATTNER, A., GOFF, L. A., ECKER, J. R. & NATHANS, J. 2018. Transcriptional and epigenomic landscapes of CNS and non-CNS vascular endothelial cells. *Elife,* 7.

SACILOTTO, N., CHOULIARAS, K. M., NIKITENKO, L. L., LU, Y. W., FRITZSCHE, M., WALLACE, M. D., NORNES, S., GARCIA-MORENO, F., PAYNE, S., BRIDGES, E., LIU, K., BIGGS, D., RATNAYAKA, I., HERBERT, S. P., MOLNAR, Z., HARRIS, A. L., DAVIES, B., BOND, G. L., BOU-GHARIOS, G., SCHWARZ, J. J. & DE VAL, S. 2016. MEF2 transcription factors are key regulators of sprouting angiogenesis. *Genes Dev,* 30**,** 2297-2309.

SAINT-GENIEZ, M., ARGENCE, C. B., KNIBIEHLER, B. & AUDIGIER, Y. 2003. The msr/apj gene encoding the apelin receptor is an early and specific marker of the venous phenotype in the retinal vasculature. *Gene Expr Patterns,* 3**,** 467-72.

SAKSOUK, N., AVVAKUMOV, N., CHAMPAGNE, K. S., HUNG, T., DOYON, Y., CAYROU, C., PAQUET, E., ULLAH, M., LANDRY, A. J., COTE, V., YANG, X. J., GOZANI, O., KUTATELADZE, T. G. & COTE, J. 2009. HBO1 HAT complexes target chromatin throughout gene coding regions via multiple PHD finger interactions with histone H3 tail. *Mol Cell*, 33**,** 257-65.

SCHINDELIN, J., ARGANDA-CARRERAS, I., FRISE, E., KAYNIG, V., LONGAIR, M., PIETZSCH, T., PREIBISCH, S., RUEDEN, C., SAALFELD, S., SCHMID, B., TINEVEZ, J. Y., WHITE, D. J., HARTENSTEIN, V., ELICEIRI, K., TOMANCAK, P. & CARDONA, A. 2012. Fiji: an open-source platform for biological-image analysis. *Nat Methods*, 9**,** 676-82.

SCIALDONE, A., NATARAJAN, K. N., SARAIVA, L. R., PROSERPIO, V., TEICHMANN, S. A., STEGLE, O., MARIONI, J. C. & BUETTNER, F. 2015. Computational assignment of cell-cycle stage from single-cell transcriptome data. *Methods*, 85**,** 54-61.

SHU, X. Z., ZHANG, L. N., ZHANG, R., ZHANG, C. J., HE, H. P., ZHOU, H., WANG, N. & ZHANG, T. C. 2015. Histone acetyltransferase p300 promotes MRTF-A-mediates transactivation of VE-cadherin gene in human umbilical vein endothelial cells. *Gene*, 563**,** 17-23.

STRASSER, G. A., KAMINKER, J. S. & TESSIER-LAVIGNE, M. 2010. Microarray analysis of retinal endothelial tip cells identifies CXCR4 as a mediator of tip cell morphology and branching. *Blood*, 115**,** 5102-10.

SU, T., STANLEY, G., SINHA, R., D'AMATO, G., DAS, S., RHEE, S., CHANG, A. H., PODURI, A., RAFTREY, B., DINH, T. T., ROPER, W. A., LI, G., QUINN, K. E., CARON, K. M., WU, S., MIQUEROL, L., BUTCHER, E. C., WEISSMAN, I., QUAKE, S. & RED-HORSE, K. 2018. Single-cell analysis of early progenitor cells that build coronary arteries. *Nature*, 559**,** 356-362.

TEAM, R. C. 2020. *R: A language and environment for statistical computing.* [Online]. Available: https://www.R-project.org/ [Accessed].

TIKHONOVA, A. N., DOLGALEV, I., HU, H., SIVARAJ, K. K., HOXHA, E., CUESTA-DOMINGUEZ, A., PINHO, S., AKHMETZYANOVA, I., GAO, J., WITKOWSKI, M., GUILLAMOT, M., GUTKIN, M. C., ZHANG, Y., MARIER, C., DIEFENBACH, C., KOUSTENI, S., HEGUY, A., ZHONG, H., FOOKSMAN, D. R., BUTLER, J. M., ECONOMIDES, A., FRENETTE, P. S., ADAMS, R. H., SATIJA,

R., TSIRIGOS, A. & AIFANTIS, I. 2019. The bone marrow microenvironment at single-cell resolution. *Nature,* 569**,** 222-228.

VANLANDEWIJCK, M., HE, L., MAE, M. A., ANDRAE, J., ANDO, K., DEL GAUDIO, F., NAHAR, K., LEBOUVIER, T., LAVINA, B., GOUVEIA, L., SUN, Y., RASCHPERGER, E., RASANEN, M., ZARB, Y., MOCHIZUKI, N., KELLER, A., LENDAHL, U. & BETSHOLTZ, C. 2018. A molecular atlas of cell types and zonation in the brain vasculature. *Nature,* 554**,** 475-480.

WANG, Y., NAKAYAMA, M., PITULESCU, M. E., SCHMIDT, T. S., BOCHENEK, M. L., SAKAKIBARA, A., ADAMS, S., DAVY, A., DEUTSCH, U., LUTHI, U., BARBERIS, A., BENJAMIN, L. E., MAKINEN, T., NOBES, C. D. & ADAMS, R. H. 2010. Ephrin-B2 controls VEGF-induced angiogenesis and lymphangiogenesis. *Nature,* 465**,** 483-6.

WANG, Z., ZANG, C., CUI, K., SCHONES, D. E., BARSKI, A., PENG, W. & ZHAO, K. 2009. Genome-wide mapping of HATs and HDACs reveals distinct functions in active and inactive genes. *Cell,* 138**,** 1019-31.

WATSON, E. C., GRANT, Z. L. & COULTAS, L. 2017. Endothelial cell apoptosis in angiogenesis and vessel regression. *Cell Mol Life Sci*.

WU, D., LIM, E., VAILLANT, F., ASSELIN-LABAT, M. L., VISVADER, J. E. & SMYTH, G. K. 2010. ROAST: rotation gene set tests for complex microarray experiments. *Bioinformatics,* 26**,** 2176-82.

WU, Z. Q. & LIU, X. 2008. Role for Plk1 phosphorylation of Hbo1 in regulation of replication licensing. *Proc Natl Acad Sci U S A,* 105**,** 1919-24.

XU, C., HASAN, S. S., SCHMIDT, I., ROCHA, S. F., PITULESCU, M. E., BUSSMANN, J., MEYEN, D., RAZ, E., ADAMS, R. H. & SIEKMANN, A. F. 2014. Arteries are formed by vein-derived endothelial tip cells. *Nat Commun,* 5**,** 5758.

XU, C. & SU, Z. 2015. Identification of cell types from single-cell transcriptomes using a novel clustering method. *Bioinformatics,* 31**,** 1974-80.

YAN, M. S., TURGEON, P. J., MAN, H. J., DUBINSKY, M. K., HO, J. J. D., EL-RASS, S., WANG, Y. D., WEN, X. Y. & MARSDEN, P. A. 2018. Histone acetyltransferase 7 (KAT7)-dependent intragenic histone acetylation regulates endothelial cell gene regulation. *J Biol Chem,* 293**,** 4381-4402.

ZHANG, B., DAY, D. S., HO, J. W., SONG, L., CAO, J., CHRISTODOULOU, D., SEIDMAN, J. G., CRAWFORD, G. E., PARK, P. J. & PU, W. T. 2013. A dynamic

H3K27ac signature identifies VEGFA-stimulated endothelial enhancers and requires EP300 activity. *Genome Res,* 23**,** 917-27.

ZHAO, Q., EICHTEN, A., PARVEEN, A., ADLER, C., HUANG, Y., WANG, W., DING, Y., ADLER, A., NEVINS, T., NI, M., WEI, Y. & THURSTON, G. 2018. Single-Cell Transcriptome Analyses Reveal Endothelial Cell Heterogeneity in Tumors and Changes following Antiangiogenic Treatment. *Cancer Res,* 78**,** 2370-2382.

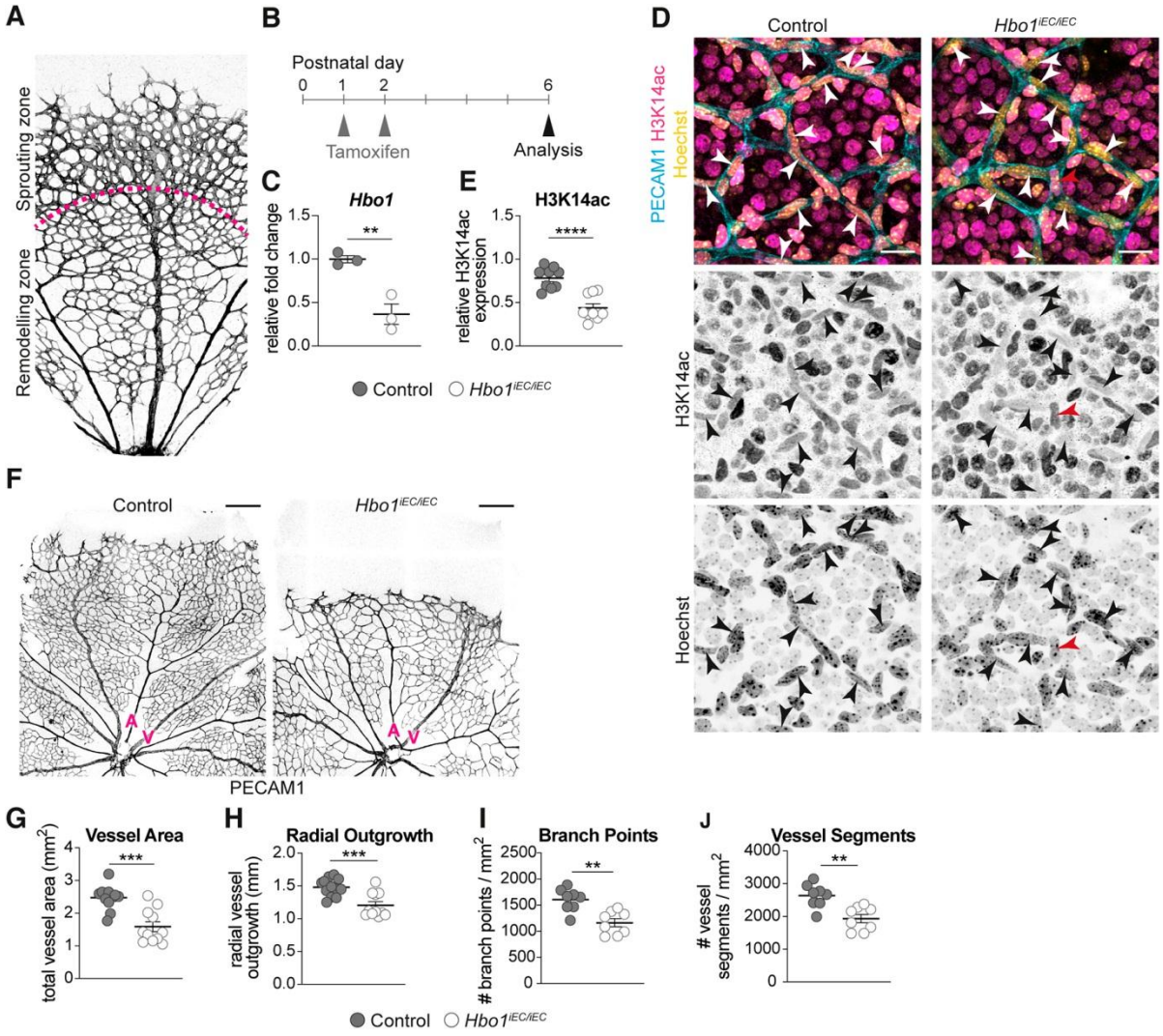

Fig. 1. Sprouting angiogenesis is impaired in the absence of HBO1

(**A**) P6 wild type retina vasculature where the pink line demarcates zones of vessel sprouting/growth and vessel remodelling. (**B**) Experimental overview for mice analysed at P6. Tamoxifen was administered at P1 and P2 to induce cre recombination of the conditional *Hbo1* allele. (**C**) qPCR analysis of *Hbo1* expression relative to *Hsp90* in lung ECs isolated from control (n = 3) and *Hbo1*$^{iEC/iEC}$ mice (n = 3) at P6. p = 0.0071. (**D**) H3K14ac (magenta) staining in P6 control and *Hbo1*$^{iEC/iEC}$ retinas. Co-stained for PECAM1 (cyan) and Hoechst 33342 (yellow). Scale bar: 20 µm. Arrowheads indicate EC nuclei. Red arrow indicates an EC from *Hbo1*$^{iEC/iEC}$ mouse that has high H3K14ac expression, which has likely escaped cre deletion of *Hbo1*. (**E**) Quantification of endothelial H3K14ac expression relative to surrounding non-ECs (control n = 9, *Hbo1*$^{iEC/iEC}$ n = 9, p<0.0001). (**F**) PECAM1 overview of P6 control and *Hbo1*$^{iEC/iEC}$ retinas. Scale bar: 500 µm. A indicates an artery, V indicates a vein. Quantification of (**G**) total retinal vessel area (control n = 11, *Hbo1*$^{iEC/iEC}$ n = 11, p =

0.0001), (**H**) radial outgrowth (control n = 12, *Hbo1*$^{iEC/iEC}$ n = 11, p = 0.0005), (**I**) branch points (control n = 8, *Hbo1*$^{iEC/iEC}$ n = 8, p = 0.0012) and (**J**) vessel segments (control n = 8, *Hbo1*$^{iEC/iEC}$ n = 8, p = 0.0016). Statistical testing by Student's two-tailed t-test. Data are mean ± SEM. Each circle represents one individual animal.

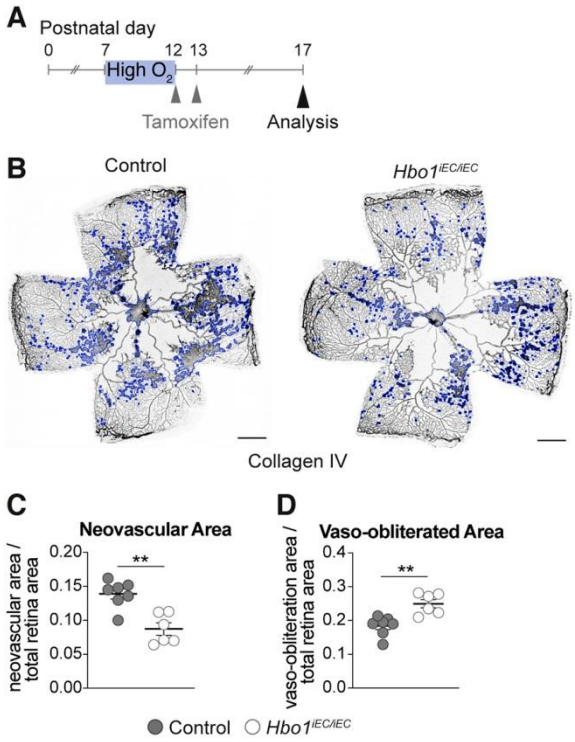

Fig. 2. HBO1 is important for pathological vessel growth

(**A**) Experimental overview of oxygen-induced retinopathy model, where mice are exposed to a high oxygen environment for five days from P7, followed by five days in room air oxygen. (**B**) Collagen IV staining of P17 control and *Hbo1*$^{iEC/iEC}$ retinas. Neovascular lesions are outlined in blue. Scale bar: 500 µm. Quantification of (**C**) neovascular area normalised to total retina area (control n = 7, *Hbo1*$^{iEC/iEC}$ n = 6, p = 0.0010) and (**D**) vaso-obliterated area normalised to total retina area at P17 (control n = 7, *Hbo1*$^{iEC/iEC}$ n = 6, p = 0.0022). Statistical testing by Student's two-tailed t-test. Data are mean ± SEM. Each circle represents one individual animal.

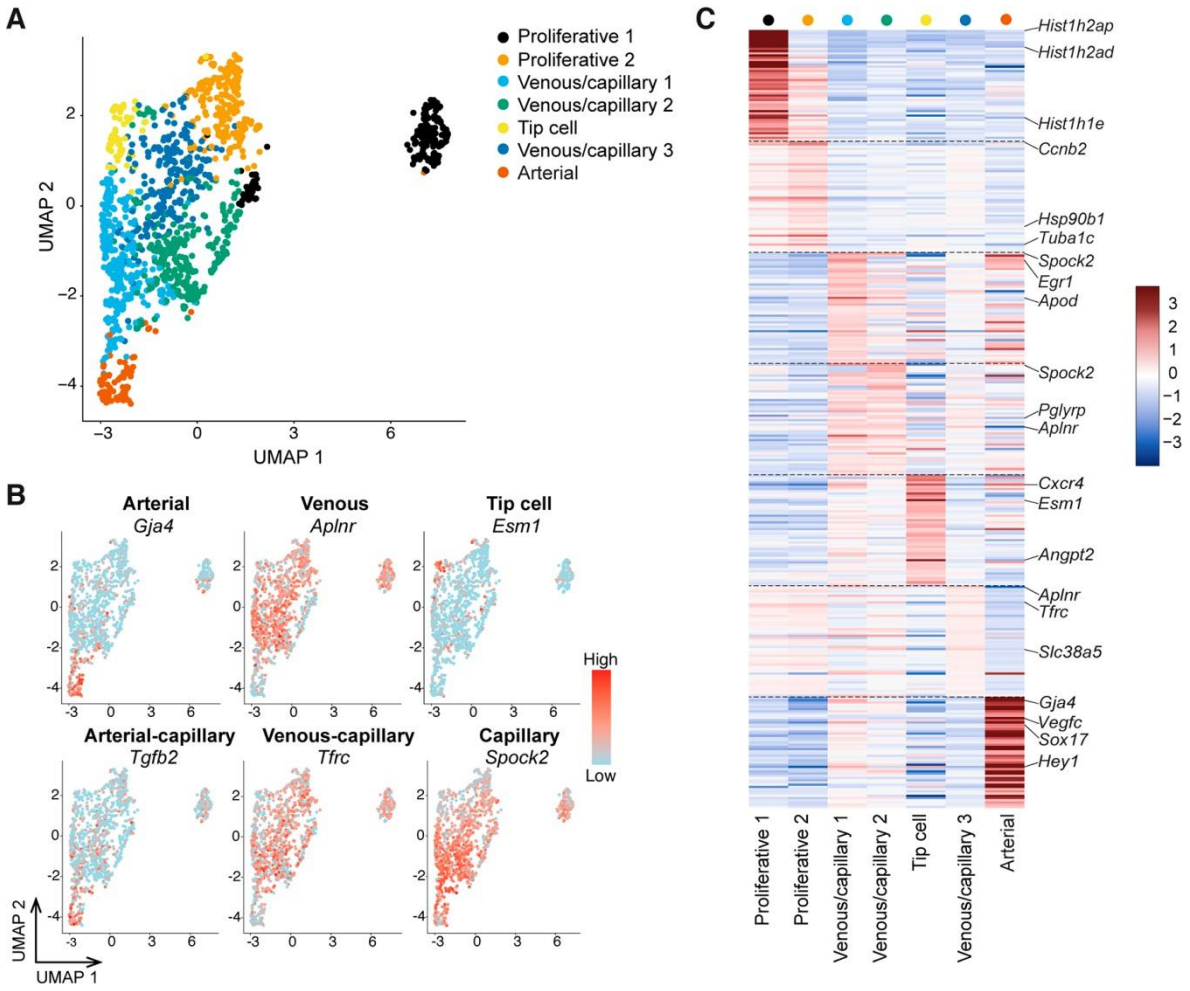

Fig. 3. Single-cell RNA sequencing of retinal ECs

(**A**) UMAP plot generated from scRNA-sequencing *Control*$^{iEC/+}$*;mTmG* and *Hbo1*$^{iEC/iEC}$*;mTmG* retinal ECs. Colour coded by cluster/EC phenotype. (**B**) UMAP plots colour-coded for expression of indicated EC phenotype marker genes. Colour scale: red = high expression, blue = low expression. (**C**) Gene-expression heatmap of top 50 marker genes per EC phenotype. Colour scale: red = high expression, blue = low expression. All figure panels samples include ECs from *Control*$^{iEC/+}$*;mTmG* n = 4, *Hbo1*$^{iEC/iEC}$*;mTmG* n = 4. Data analysed as described in the Materials and Methods.

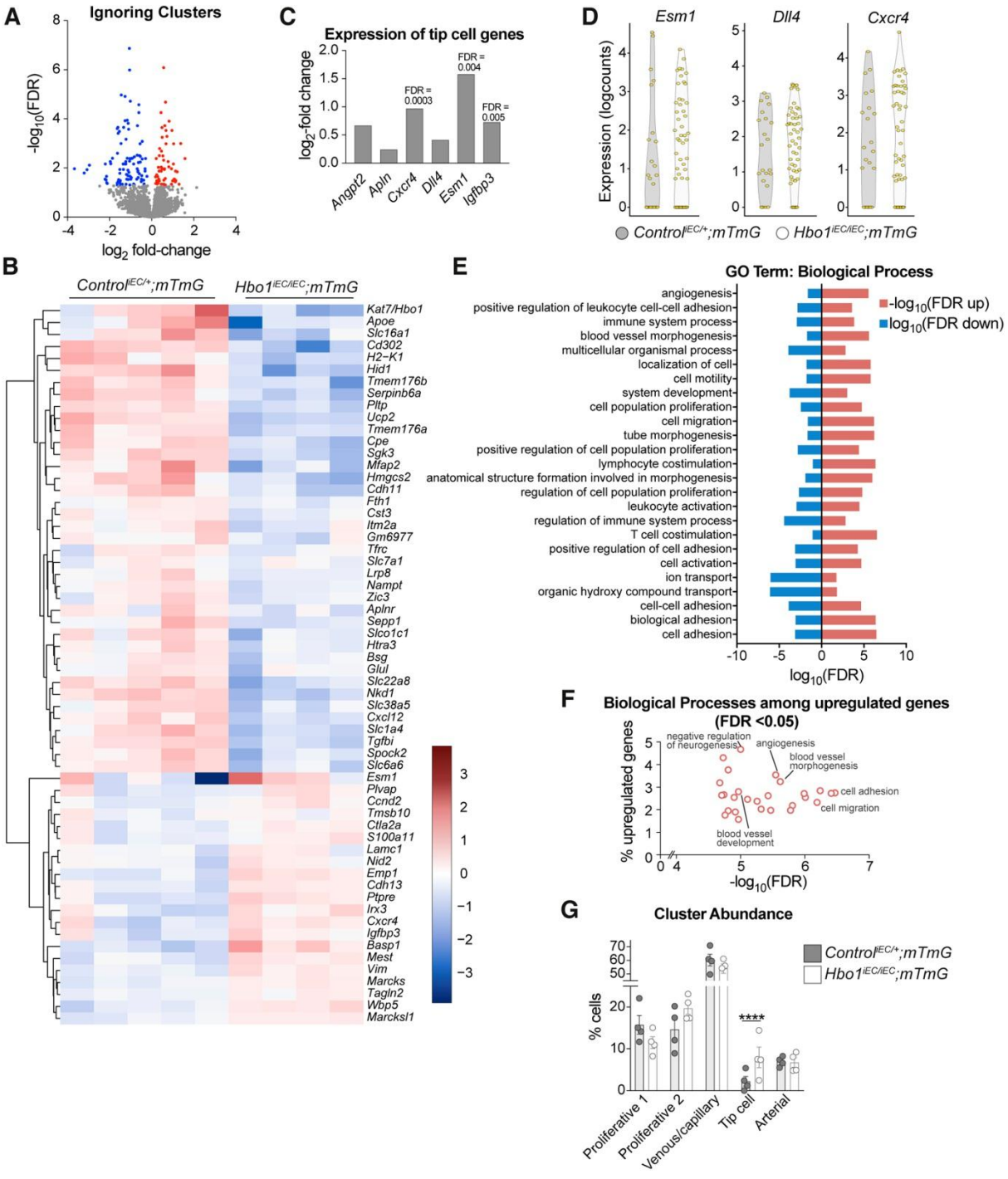

Fig. 4. Tip cells are over-represented in the absence of HBO1

(**A**) Volcano plot showing expression changes for all genes ignoring cluster labels. Genes that are significantly differentially expressed (FDR <0.05) in *Hbo1*$^{iEC/iEC}$*;mTmG* retinal ECs compared to *Control*$^{iEC/+}$*;mTmG* ECs are indicated: Red = upregulated; blue = downregulated; grey = not significant. (**B**) Gene expression heatmap of the top 60 differentially expressed genes (FDR < 0.05) when ignoring clusters in *Hbo1*$^{iEC/iEC}$*;mTmG* retinal ECs relative to *Control*$^{iEC/+}$*;mTmG*. Shows log-expression values normalised to the

mean of all samples in filtered dataset. Rows correspond to genes, columns to sample. Colour scale: red = high expression, blue = low expression. (**C**) mRNA levels of tip cell expressed genes in *Hbo1*$^{iEC/iEC}$*;mTmG* retinal ECs relative to *Control*$^{iEC/+}$*;mTmG*. (**D**) Violin plots of tip cell gene marker expression within tip cell cluster for *Control*$^{iEC/+}$*;mTmG* and *Hbo1*$^{iEC/iEC}$*;mTmG* mice. Each circle indicates the expression (logcounts) for a single cell. For expression across all clusters see Fig. S5E. (**E**) Top 25 most differentially expressed biological processes gene ontology (GO) terms in *Hbo1*$^{iEC/iEC}$*;mTmG* ECs compared to *Control*$^{iEC/+}$*;mTmG*. The $\log_{10}$ value for the up- (red, shows the -$\log_{10}$ value) and downregulated (blue) FDR associated with each term is shown. All terms are FDR<0.05. For full list of genes associated with each term see Supp Table 3. (**F**) Scatterplot of the top 30 significantly upregulated biological processes GO terms in *Hbo1*$^{iEC/iEC}$*;mTmG* ECs compared to *Control*$^{iEC/+}$*;mTmG*. Each dot represents the significance of one biological process against the proportion of genes associated with that term that are upregulated in *Hbo1*$^{iEC/iEC}$*;mTmG* ECs compared to controls. This figure excludes GO terms that have a total of fewer than 15 genes per annotation. For the full list of terms see Supp Table 3. (**G**) Relative abundance of ECs within each cluster for *Control*$^{iEC/+}$*;mTmG* and *Hbo1*$^{iEC/iEC}$*;mTmG* mice, data are mean ± SEM, ****FDR<0.0001. All figure panels from scRNA-seq data and samples include ECs from *Control*$^{iEC/+}$*;mTmG* n = 4, *Hbo1*$^{iEC/iEC}$*;mTmG* n = 4. Data analysed as described in Materials and Methods.

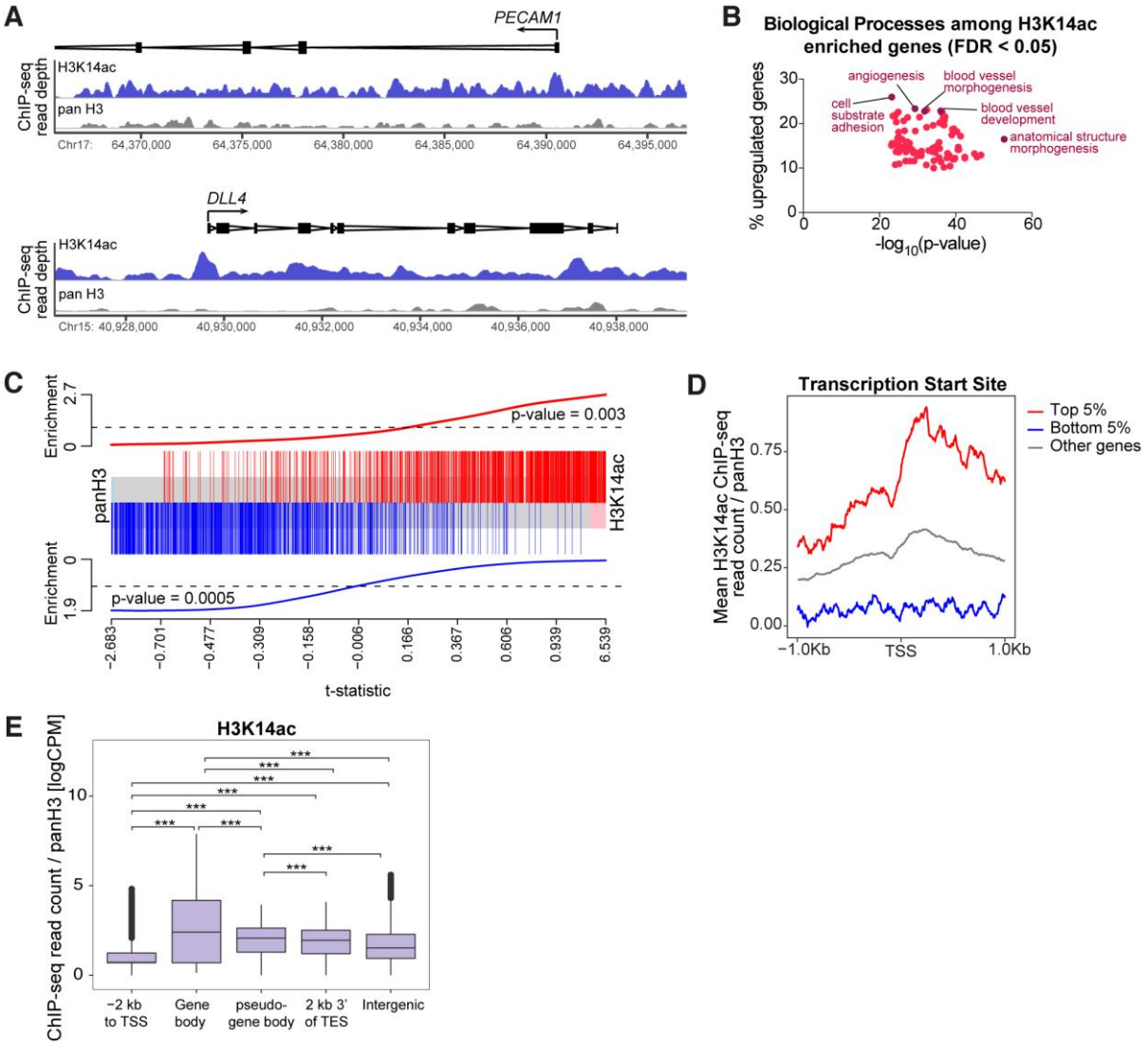

Fig. 5. H3K14ac is widely distributed across the endothelial genome and enriched at genes required for angiogenesis.

(**A**) Read depth plot of H3K14ac (blue) and pan H3 (grey) as assessed by ChIP-seq in HUVECs at the transcription start sites (TSS) of the *PECAM1* and *DLL4* locus. H3K14ac ChIP samples were sequenced with twice the depth as pan H3 samples as described in methods. (**B**) Scatterplot of the top 100 biological processes GO terms of genes enriched for H3K14ac (n = 3) over pan H3 (n = 2). Each dot represents the significance of one biological process against the percentage of genes associated with that process that are enriched for H3K14ac. For full list of GO terms see Supp Table 5. (**C**) Barcode plot displaying the top 5% (red vertical lines) and bottom 5% (blue vertical lines) genes expressed by HUVECs (Zhang et al., 2013) over genes enriched or depleted for H3K14ac by ChIP. ChIP-seq reads from the TSS to TSS+1kb are indicated by the light blue, grey and pink boxes. Genes that are enriched

for H3K14ac over pan H3 are represented on the right-hand side of the barcode (pink box indicates FDR<0.05) and reads enriched in pan H3 more so than H3K14ac are represented on the left-hand side of the barcode (blue box indicates FDR<0.05). The black dotted horizontal lines indicate what is considered neutral or no enrichment. The red worm at the top indicates that genes highly expressed in HUVECs are enriched for H3K14ac (p=0.003) and the blue worm at the bottom indicates that genes lowly expressed in HUVECs are depleted for H3K14ac (p=0.0005). (**D**) H3K14ac occupancy as ChIP-seq read counts normalised to pan H3 in gene TSS±1 kb and segregated by expression level into top 5% (red line), intermediate 90% (grey line) and bottom 5% (blue line) in HUVECs based on RNA-seq data by Zhang *et al* (Zhang et al., 2013). (**E**) Boxplots of H3K14ac occupancy as ChIP-seq read counts at various genomic features (1^{st} quartile, median and 3^{rd} quartile of the distributions define the boxes, outliers are indicated by dots). Intergenic regions are defined as ≥10 kb away from any gene. TES = transcription end site. H3K14ac n = 3, pan H3 n = 2, input n = 2. Data were analysed as described in Materials and Methods.

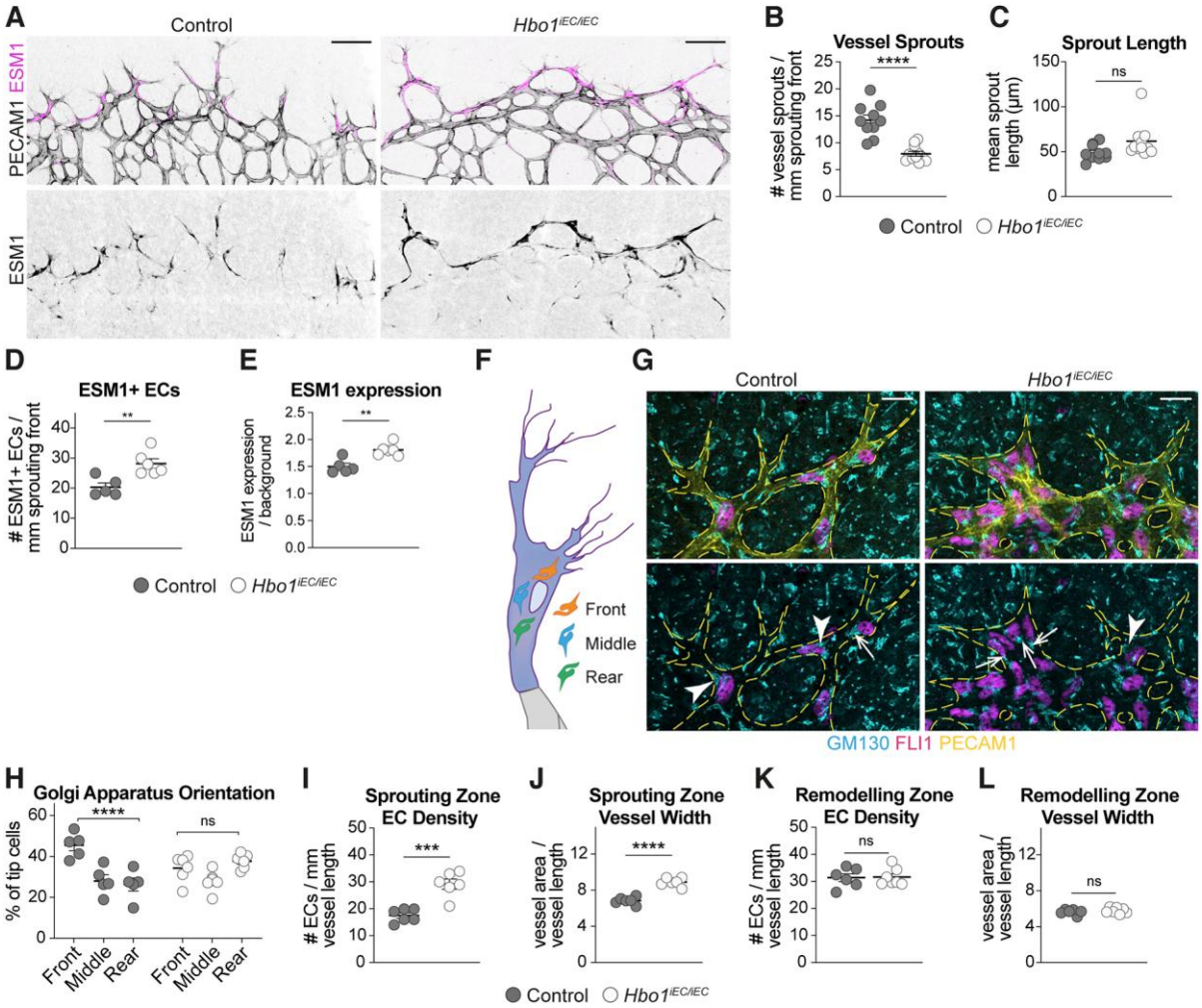

Fig. 6. Tip cells are specified normally in the absence of HBO1 but have impaired front-rear polarity

(**A**) Vessels in the sprouting front of P6 control and *Hbo1*$^{iEC/iEC}$ retinas stained for PECAM1 (greyscale) and tip cell marker ESM1 (magenta). Scale bar: 80 µm. Quantification of (**B**) vessel sprouts (control n = 10, *Hbo1*$^{iEC/iEC}$ retinas n = 11, p<0.0001), (**C**) average sprout length (control n = 10, *Hbo1*$^{iEC/iEC}$ retinas n = 11, p = 0.066), (**D**) the number of ESM1+ ECs per length of sprouting front (control n = 5, *Hbo1*$^{iEC/iEC}$ retinas n = 6, p = 0.0054) and (**E**) ESM1 expression above background in ESM1+ cells (control n = 5, *Hbo1*$^{iEC/iEC}$ retinas n = 6, p = 0.0024). (**F**) Tip cells establish front-rear polarity by orientating their Golgi apparatus in front of the nucleus with respect to the sprouting/leading edge of the cell (shown by orange shape). Tip cells may alternatively orientate their Golgi apparatus to the middle of the nucleus (blue) or behind the nucleus (green) with respect to sprouting edge. (**G**) P6 control and *Hbo1*$^{iEC/iEC}$ tip cells stained for Golgi apparatus marker GM130 (cyan), FLI1 (magenta) and PECAM1 (yellow). Scale bar: 20 µm. Arrowheads indicate front polarised tip cells,

arrows indicate rear polarised ECs. (**H**) Proportion of ESM1+ tip cells polarised in each direction for control (n = 5) and *Hbo1*$^{iEC/iEC}$ (n = 6) mice. Two-way ANOVA with Tukey's multiple comparisons test, ns p = 0.5811, ****p<0.0001. Quantification of (**I**) EC density within vessels at the edge of sprouting front (control n = 6, *Hbo1*$^{iEC/iEC}$ n = 6, p =0.0003), (**J**) vessel width at the edge of sprouting front (control n = 6, *Hbo1*$^{iEC/iEC}$ n = 6, p<0.0001), (**K**) EC density within vessels in the remodelling zone (control n = 6, *Hbo1*$^{iEC/iEC}$ n = 7, p = 0.90) and (**L**) vessel width in the remodelling zone (control n = 6, *Hbo1*$^{iEC/iEC}$ n = 7, p = 0.41). Statistical testing by Student's two-tailed t-test (except where indicated in **H**). Data are mean ± SEM. Each circle represents one individual animal.

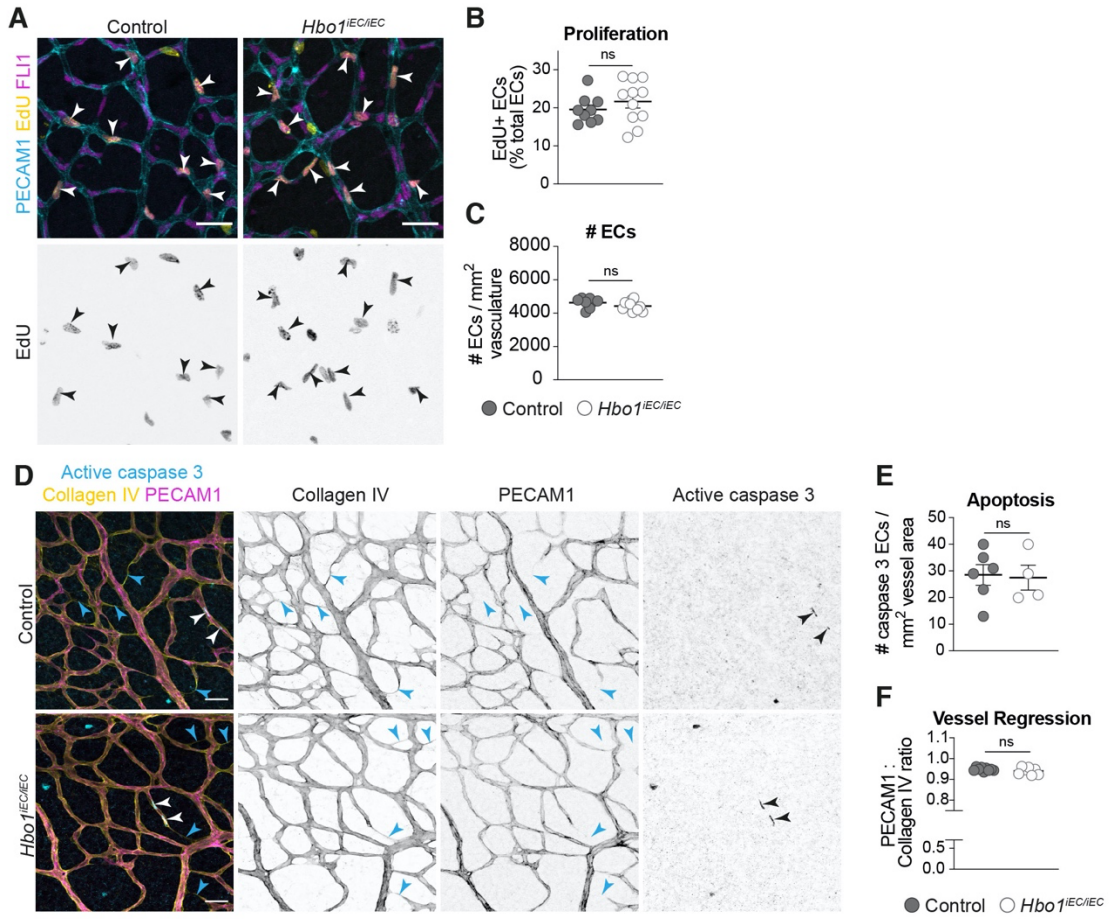

Fig. S1. Vessel patterning, EC Proliferation, EC apoptosis and vessel regression are normal in the absence of HBO1

(**A**) Proliferating ECs (indicated by arrowheads) in P6 control and *Hbo1*$^{iEC/iEC}$ retinas within the sprouting zone capillaries stained for PECAM1 (cyan), endothelial nuclear marker FLI1 (magenta) and EdU (yellow). Scale bar: 30 µm. Quantification of (**B**) proportion of proliferating ECs (control n = 9, *Hbo1*$^{iEC/iEC}$ n = 11, p = 0.35), (**C**) number of ECs per vessel area across whole retina (control n = 8, *Hbo1*$^{iEC/iEC}$ n = 11, p = 0.16). (**D**) P6 retinas from control and *Hbo1*$^{iEC/iEC}$ mice stained with collagen IV (yellow), PECAM1 (magenta) and active caspase 3 (cyan). Blue arrows indicate regressing vessels (PECAM1^{-} collagen IV^{+}) and white arrows indicate apoptotic ECs. Scale bar: 40 µm. Quantification of (**E**) apoptotic ECs per vessel area (control n = 6, *Hbo1*$^{iEC/iEC}$ n = 4, p = 0.87) and (**F**) vessel regression across retina (control n = 9, *Hbo1*$^{iEC/iEC}$ n = 7, p = 0.25) in P6 retinas. All statistical testing by Student's two-tailed t-test. All data are mean ± SEM. Each circle represents one individual animal.

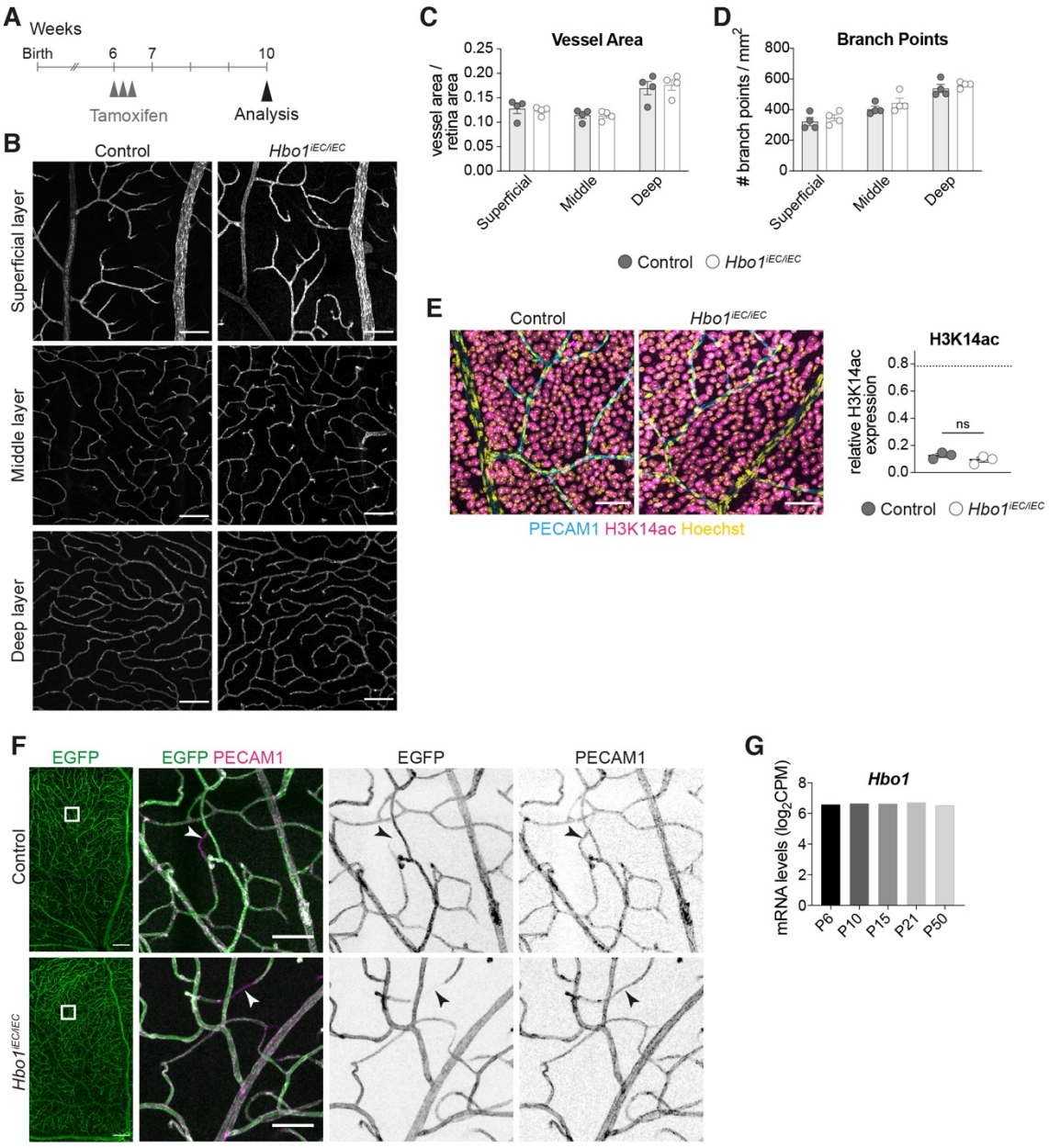

Fig. S2. Loss of HBO1 does not affect adult vasculature.

(**A**) Experimental overview for adult mice. Tamoxifen was administered for three consecutive days at six weeks of age and mice were analysed at ten weeks. (**B**) PECAM1 staining in superficial, middle and deep vessel layers of control and *Hbo1*$^{iEC/iEC}$ adults. Scale bar: 80 µm. Quantification of (**C**) vessel area per retina area for each vessel layer (control n = 4, *Hbo1*$^{iEC/iEC}$ n = 4) and (**D**) branch points (control n = 4, *Hbo1*$^{iEC/iEC}$ n = 4). (**E**) H3K14ac (magenta) staining and quantification in control (n = 9) and *Hbo1*$^{iEC/iEC}$ (n = 9) adult retinas. Co-stained for PECAM1 (cyan) and Hoechst 33342 (yellow). Scale bar: 50 µm. Dashed line indicates relative H3K14ac expression of P6 control mice, shown originally in Figure 1E. Student's two-tailed t-test, p = 0.22. (**F**) EGFP (green) and PECAM1 (magenta) in adult control and *Hbo1*$^{iEC/iEC}$ mice. White box in left-hand image enlarged in right-hand images. Scale bar: 200 µm (left)

and 50 µm (right). White/black arrows indicate EGFP$^-$ ECs. (**G**) Mean *Hbo1* mRNA expression (log_2 counts per million) in retinal ECs from P6 – P50 as analysed in data from Jeong *et al*[1]. Except in *G*, all data are mean ± SEM. Each circle represents one individual animal.

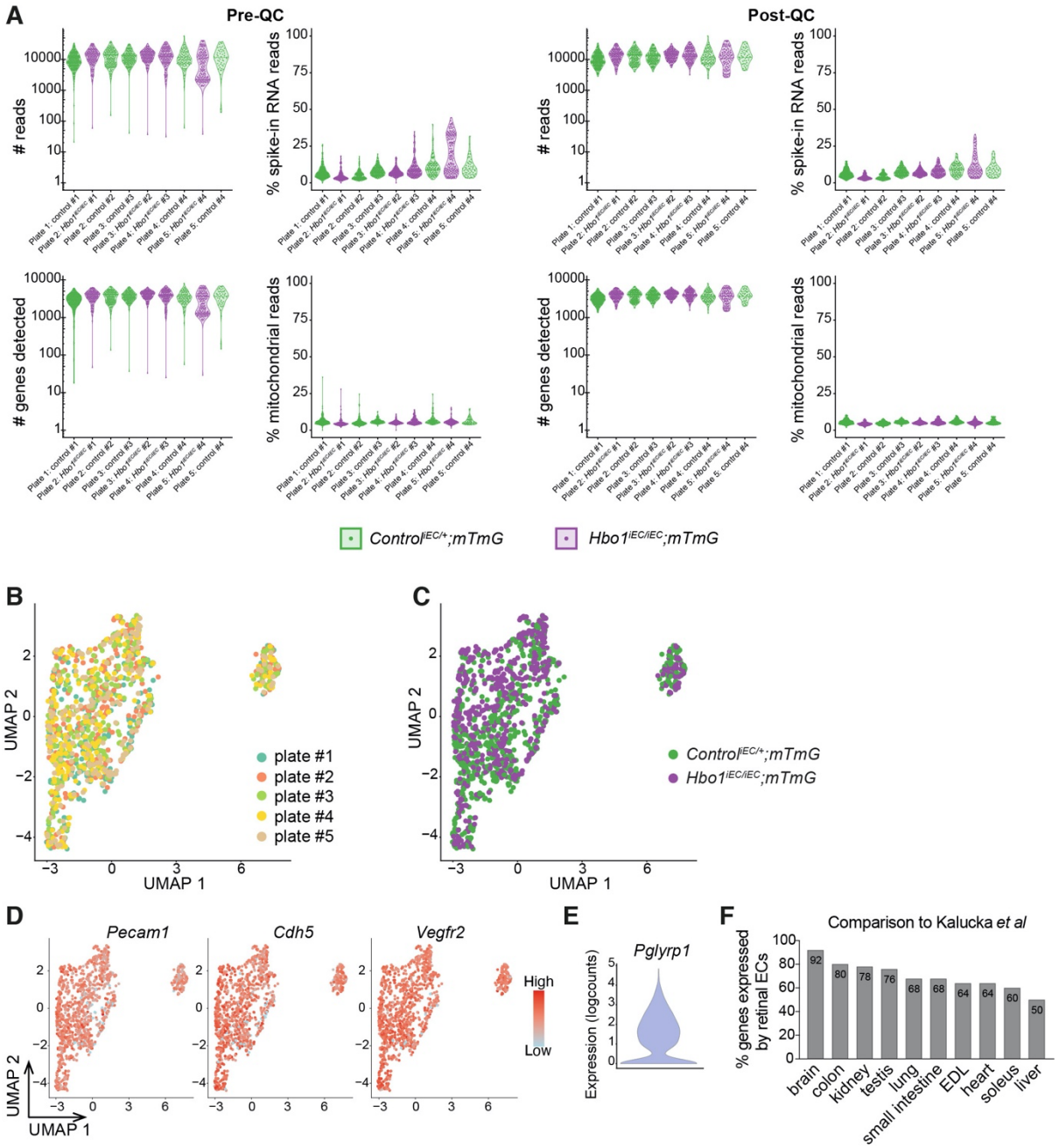

Fig. S3. Quality controls for scRNA-seq of retinal ECs.

(**A**) Violin plots of total number of reads, total number of genes detected, proportion of reads mapped to spike-in RNA and proportion of reads mapped to mitochondrial genes before and after cells that failed to achieve quality control (QC) cut-offs were removed from the analysis. See Table S6 for QC cut-offs. (**B**) UMAP plot colour coded for batch/plate analysed and (**C**) genotype (*Control*$^{iEC/+}$*;mTmG* n = 4, *Hbo1*$^{iEC/iEC}$*;mTmG* mice n = 4). (**D**) UMAP plots colour-coded for expression of indicated endothelial genes. Colour scale: red = high expression, blue = low expression. (**E**) Violin plot of *Pglyrp1* expression across all ECs sequenced and analysed. (**F**) Proportion (value shown on bar plot) of the top 50 tissue specific capillary markers from

Kalucka *et al*[2] that are expressed by retinal ECs. EDL: extensor digitorum longus skeletal muscle. All figure panels from scRNA-seq data and samples include ECs from *Control*$^{iEC/+}$*;mTmG* n = 4, *Hbo1*$^{iEC/iEC}$*;mTmG* n = 4. Data were analysed as described in the Material and Methods section.

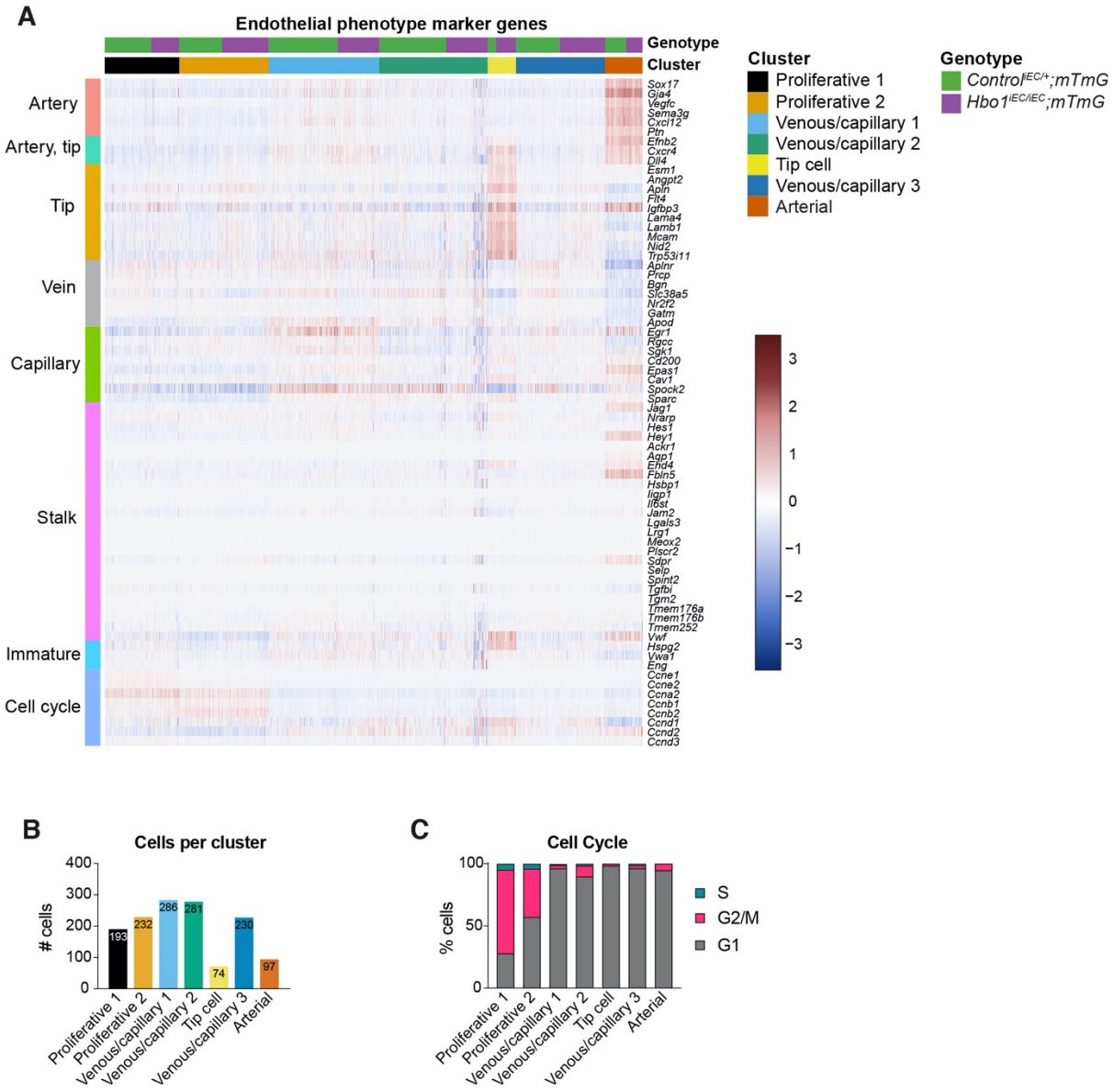

Fig. S4. Intratissue heterogeneity of retinal ECs.

(**A**) Heatmap displaying batch corrected logcounts (row-normalised) for EC subtype marker genes from Kalucka *et al*[2], Goveia *et al*[3] and Zhao *et al*[4]. Colour scale: red = high expression, blue = low expression. (**B**) Total number of cells within each cluster (includes both *Control*$^{iEC/+}$*;mTmG* and *Hbo1*$^{iEC/iEC}$*;mTmG* mice). Number of cells indicated on bar plot. (**C**) Proportion of cells in each cluster in each stage of the cell cycle as determined by cyclone classifier analysis. All figure panels from scRNA-seq data and samples include ECs from *Control*$^{iEC/+}$*;mTmG* n = 4, *Hbo1*$^{iEC/iEC}$*;mTmG* n = 4. Data were analysed as described in the Material and Methods section.

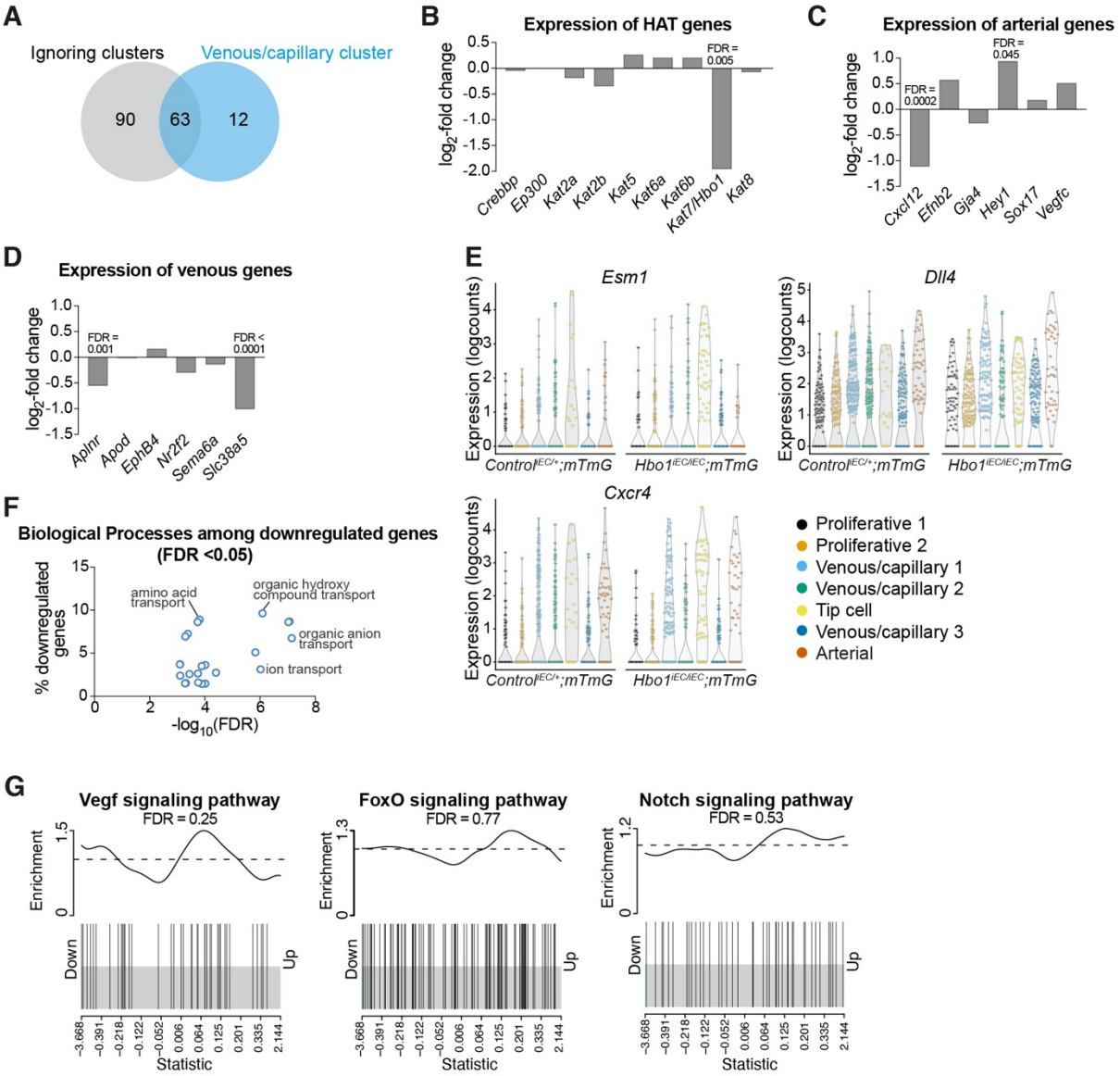

Fig. S5. Deletion of *Hbo1* causes changes in retinal EC gene expression.

(**A**) Overlap between differentially expressed genes ignoring clusters and in the venous/capillary clusters. mRNA levels of genes (**B**) encoding histone acetyltransferases, (**C**) expressed by arterial ECs and (**D**) expressed by venous ECs in *Hbo1*$^{iEC/iEC}$*;mTmG* retinal ECs relative to *Control*$^{iEC/+}$*;mTmG*. (**E**) Violin plots of tip cell gene marker expression across all clusters for *Control*$^{iEC/+}$*;mTmG* and *Hbo1*$^{iEC/iEC}$*;mTmG* mice. Each circle indicates the expression (in logcounts) for a single cell. (**F**) Scatterplot of the top 30 significantly downregulated biological processes GO terms in *Hbo1*$^{iEC/iEC}$*;mTmG* ECs compared to *Control*$^{iEC/+}$*;mTmG*. Each dot represents the significance of one biological process against the proportion of genes associated with that term that are downregulated in *Hbo1*$^{iEC/iEC}$*;mTmG* ECs compared to *Control*$^{iEC/+}$*;mTmG*. This figure excludes GO terms that have a total of fewer than 25 genes per annotation. For the full list of terms see Supp Table 3. (**G**) Barcode plots showing

enrichment of indicated pathways in *Hbo1*$^{iEC/iEC}$ retinal ECs compared to control. The vertical lines ('barcode') represent all pathway genes expressed in the ECs. At the top, the horizontal dotted line represents what is considered neutral or no enrichment and worm represents the enrichment of pathway genes in *Hbo1*$^{iEC/iEC}$ ECs. FDR was calculated by rotation gene set tests, testing whether the gene set is differentially expressed in either direction. All figure panels from scRNA-seq data and samples include ECs from *Control*$^{iEC/+}$*;mTmG* n = 4, *Hbo1*$^{iEC/iEC}$*;mTmG* n = 4. Data were analysed as described in the Material and Methods section.

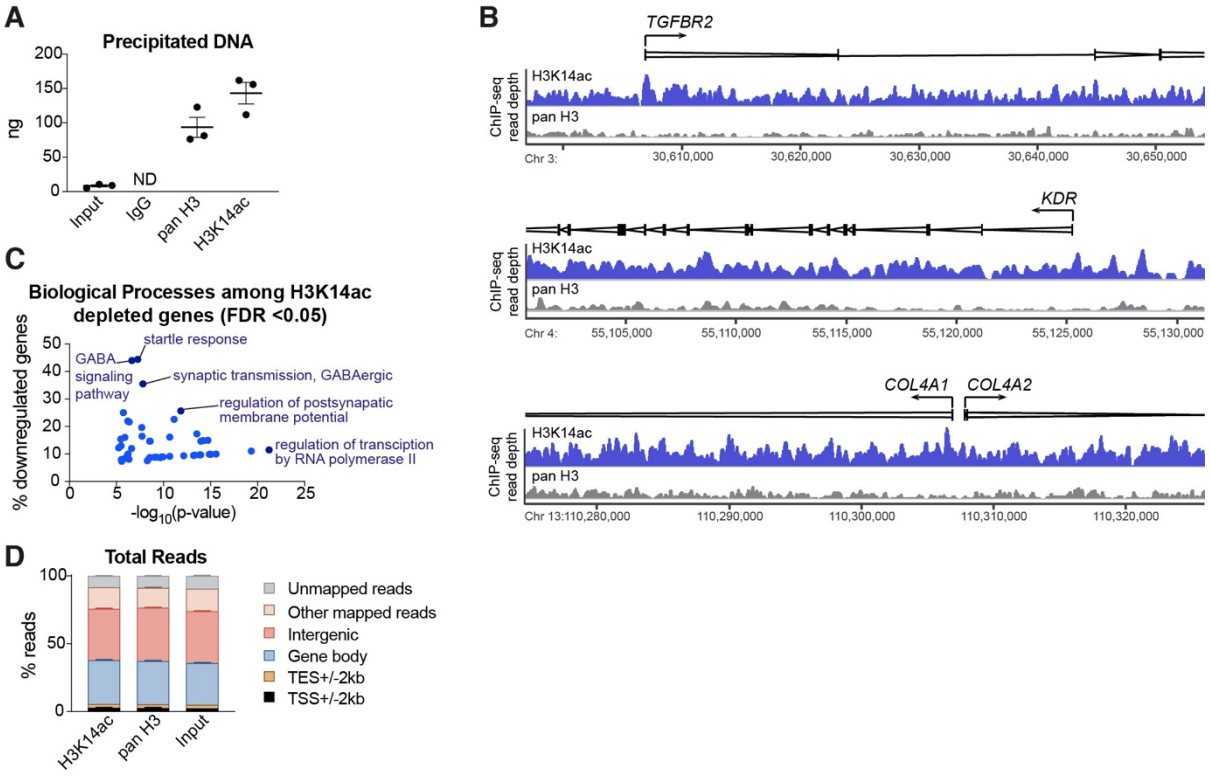

Fig. S6. H3K14ac is widely distributed in the endothelial cell genome.

(**A**) Total DNA precipitated by ChIP, ND = not detected. Data are mean ± SEM. Each circle represents one sample (n = 3). (**B**) Read depth plot of H3K14ac (blue) and pan H3 (grey) as assessed by ChIP-seq in HUVECs at the transcription start sites (TSS) of *TGFBR2, KDR, COL4A1* and *COL4A2* loci. H3K14ac samples were sequenced with twice the depth as pan H3 samples as described in methods. (**C**) Scatterplot of the top 100 biological processes GO terms at genes depleted for H3K14ac (n = 3) compared to pan H3 (n = 2). Each dot represents the significance of one biological process against the percentage of genes associated with that process that are depleted for H3K14ac. For the full list of GO terms see Supp Table 5. (**D**) Proportion of total reads that were mapped to the human genome and those that correspond to intergenic regions (defined as ≥10 kb away from any gene), gene bodies, TSS ± 2 kb and transcription end sites (TES) ± 2 kb. H3K14ac n = 3, pan H3 n = 2, input n = 2. Data are mean ± SEM. Data were analysed as described in the Material and Methods section.

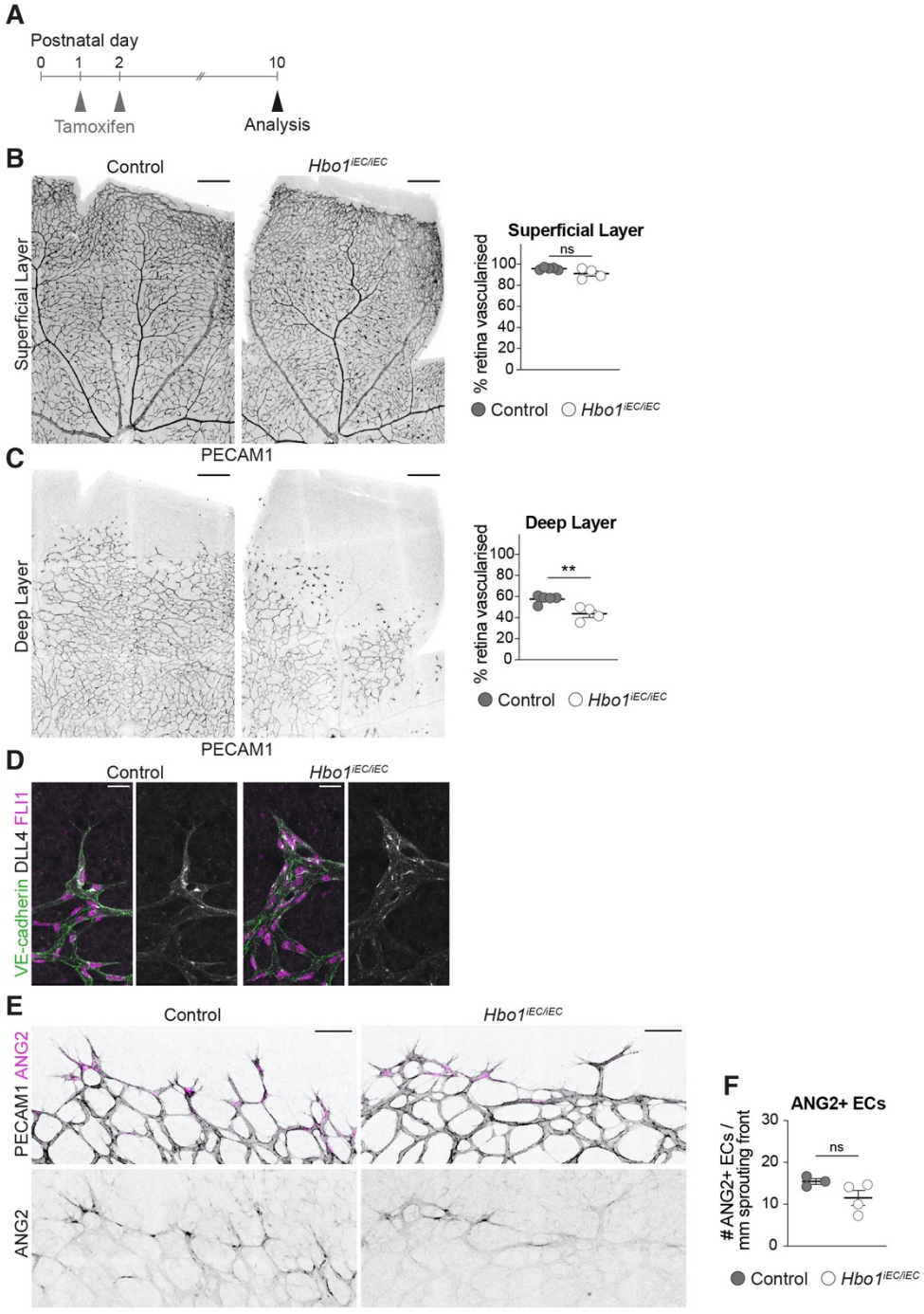

Fig. S7. Loss of HBO1 impairs sprouting into deeper retinal vessel layers.

(**A**) Experimental overview for mice analysed at P10. Tamoxifen was administered at P1 and P2 to induce cre recombination. (**B**) PECAM1 staining and quantification of proportion of the superficial retina vascularised in P10 retinas (control n = 5, *Hbo1*$^{iEC/iEC}$ n = 4, p = 0.067). (**C**) PECAM1 staining and quantification of proportion of the deep retina vascularised in P10 retinas (control n = 5, *Hbo1*$^{iEC/iEC}$ n = 4, p = 0.005). (**D**) Representative example of DLL4 expression (grey) in tip cells of control and *Hbo1*$^{iEC/iEC}$ retinas. Retinas also stained with VE-cadherin (green) and FLI1 (magenta). Scale bar: 30 µm. (**E**) Vessels in the sprouting front of

P6 control and *Hbo1*$^{iEC/iEC}$ retinas stained for PECAM1 (greyscale) and tip-cell marker ANG2 (magenta). Scale bar: 80 µm. (**F**) Quantification of the number of ANG2+ ECs per length of sprouting front (control n = 3, *Hbo1*$^{iEC/iEC}$ retinas n = 4, p = 0.13). All statistical testing by Student's two-tailed t-test. All data are mean ± SEM. Each circle represents one individual animal.

Table S1. Retinal scRNA-seq cluster marker genes

Click here to download Table S1

Table S2. Differentially expressed genes in Hbo1 deleted ECs by scRNA-seq Supplementary

Click here to download Table S2

Table S3. Gene Ontology terms (biological processes) upregulated and downregulated in Hbo1 deleted ECs by scRNA-seq

Click here to download Table S3

Table S4. Genes enriched or depleted for H3K14ac

Click here to download Table S4

Table S5. Gene Ontology terms (biological processes) for H3K14ac enriched and depleted gene bodies by ChIP-seq

Click here to download Table S5

Table S6. Retinal EC scRNA-seq quality control metrics

Click here to download Table S6

Supplementary Data References

1 Jeong, H. W. *et al.* Transcriptional regulation of endothelial cell behavior during sprouting angiogenesis. *Nat Commun* **8**, 726, doi:10.1038/s41467-017-00738-7 (2017).

2 Kalucka, J. *et al.* Single-Cell Transcriptome Atlas of Murine Endothelial Cells. *Cell* **180**, 764-779 e720, doi:10.1016/j.cell.2020.01.015 (2020).

3 Goveia, J. *et al.* An Integrated Gene Expression Landscape Profiling Approach to Identify Lung Tumor Endothelial Cell Heterogeneity and Angiogenic Candidates. *Cancer Cell* **37**, 21-36 e13, doi:10.1016/j.ccell.2019.12.001 (2020).

4 Zhao, Q. *et al.* Single-Cell Transcriptome Analyses Reveal Endothelial Cell Heterogeneity in Tumors and Changes following Antiangiogenic Treatment. *Cancer Res* **78**, 2370-2382, doi:10.1158/0008-5472.CAN-17-2728 (2018).